

# Numerical Simulation of Vortex Pyrolysis Reactors for Condensable Tar Production from Biomass

R.S. MILLER and J. BELLAN<sup>†</sup>

Jet Propulsion Laboratory, California Institute of Technology, Pasadena, CA 91109-8099

<sup>†</sup> *Author for correspondence; jbellan@jpl.nasa.gov*

A numerical study is performed in order to evaluate the performance and optimal operating conditions of **vortex** pyrolysis reactors used for condensable tar production from biomass. A detailed mathematical model of porous biomass particle pyrolysis is coupled with a compressible Reynolds stress transport model for the **turbulent** reactor swirling flow. An initial evaluation of particle **dimensionality** effects is made through comparisons of single- **(1D)** and **multi-dimensional** particle simulations and reveals that the **1D** particle model results in **conservative** estimates for total pyrolysis conversion times and tar collection. The observed deviations are due predominantly to geometry effects while directional effects from thermal conductivity and permeability variations **are** relatively **small**. Rapid ablative particle heating rates are attributed to a mechanical fragmentation of the biomass particles that is modeled using a critical porosity for matrix breakup. Optimal thermal conditions for tar production are **observed** for reactor wall temperatures of approximately **900K**. Effects of biomass identity, particle size **distribution**, and reactor **geometry** and scale **are** discussed

## 1 INTRODUCTION

Among the pyrolysis reactor designs investigated for commercial production of condensable tars *from* biomass, the vortex reactor is a potentially efficient configuration due to the rapid **particle** heating rates achieved through direct-contact **ablation**.<sup>[1]</sup> The vortex reactor is characterized by a strongly swirling flow of superheated steam through a cylindrical reactor that creates a centrifugal acceleration which results in the injected biomass particles maintaining direct-contact with a high temperature outer wall. Biomass tars and gases resulting from the pyrolysis are then removed **from** the reactor through a central exit pipe whereas partially pyrolyzed material is **re-entrained** using a separate recycle loop resulting in complete reaction of the particles. To prevent the degradation of product tars within the reactor, it is important to achieve **small** residence times for the gaseous pyrolysis products. **The** condensed high molecular weight tars are collected and quenched, and the exit gases are later used in a variety

of applications including hydrogen **fuel production**.<sup>[2]</sup> In spite of the attractive nature of the design, there are no thorough analyses of **vortex** pyrolysis reactors addressing the crucial issues of efficiency, optimal **operating** conditions and **scale up** for commercial use.

Previous investigations of **vortex** biomass pyrolysis **reactors** have been confined primarily to small scale experiments and limited global **modeling**. Such investigations have been performed by **Diebold and Power**<sup>[1]</sup> utilizing a reactor  $\sim 1m$  in length with a wall temperature of approximately  $900K$  and measured mass feed rates up to  $30kg/hr$ . The reactor efficiency was observed to be enhanced by inserting a narrow pitch groove on the inside wall of the reactor in order to increase the particle residence times, Despite the **fact** that no quantitative experimental measurements were reported, their analysis suggests that the **configuration** is capable of efficiently pyrolyzing biomass for conversion to condensable tars and no limitations on scaling for commercial usage were observed. Quantitative measurements, parameter studies and mathematical optimization are the next necessary step before commercial use can be considered.

Although the literature addressing the vortex reactor is limited, previous investigations of different types of ablative reactor designs exist lending support to the potential of fast pyrolysis. While most reactors have been utilized in bench scale experiments, few have been shown to be viable for scale up to commercial sizes. These reactors **generally** employ a combination of **direct-contact** between the biomass particles and the heated surface in conjunction with mechanical breakup or grinding of the particles to **further** increase heating rates. The 'rotating cone' flash pyrolysis reactor is similar in design to the vortex reactor and was considered by **Wagenaar et. al.** <sup>[3]</sup>; however, only for 'cold flow' conditions. **Peacocke and Bridgwater**<sup>[4]</sup> recently proposed an as yet untested ablative reactor design in which a four blade arrangement is used to apply the biomass particles directly to a hot **surface** under high relative velocity and pressure. Currently, published work for **all** of the above reactor types is relatively limited and many questions remain before **actual** commercial applications **are** viable. In particular, **further** research is needed to determine the efficiency of **direct-contact** pyrolysis, effects of ablative pyrolysis, optimal reactor **temperatures**, effects of the turbulent gas flow field, and range of particle sizes which can be

economically pyrolyzed.

In this paper we present quantitative results from numerical simulations of **full** scale vortex reactors under viable operating conditions obtained from **detailed** mathematical models including a realistic formulation for the turbulent carrier gas flow field. Of particular interest **are the** identification and elucidation of pertinent physical processes as well as a quantitative assessment of parameter effects, optimal conditions and scaling potential. Specifics of the vortex reactor and its sub-models are addressed in Section 2. Single particle simulation results are presented in Section 3. Here we address the issues of particle dimensionality, wall heating, the response of the particle equations to temporal oscillations in the **free** stream **boundary conditions**, and the introduction of a new fragmentation model needed to describe the mechanical break up of particles. Section 4 describes the coupling of sub-models and contains the reactor simulation results and parametric studies; the parameters being the wall temperature, feed rate, feed stock, particle size distribution and reactor scaling. Conclusions and **further** discussions are provided in Section 5.

## 2 VORTEX REACTOR AND SUB-MODEL FORMULATION

Figure 1 provides a schematic illustration of the modeled vortex reactor. The design is an approximation of the experimental facility at the National Renewable Energy Laboratory (**NREL**) (note that the NREL reactor has been modified but not yet documented, since the publication of **Ref.<sup>[1]</sup>**). A high **temperature** steam carrier gas is mixed with a biomass feed **upstream** of the inflow pipe. The mixture is then introduced tangentially into the reactor at high velocity creating a strongly swirling flow whereby the particles are centrifuged against the wall and remain primarily in direct sliding contact with the heated constant temperature **surface.<sup>[1]</sup>** Steam and resulting gaseous pyrolysis products then exit the reactor through an outflow of specified diameter whereas partially pyrolyzed particles **are re-entrained** through a **small** tangential recycle loop (not shown). The present investigation aims at modeling the steady state reactor operation. The modeling is accomplished through the coupling of sub-models for the individual particle pyrolysis, the turbulent swirling flow and the particle trajectories along the outer ( $r = R_R$ )

heated wall.

## 2.1 Particle *Pyrolysis Model*

The individual macro-particle pyrolysis is based on the detailed model of Miller and Bellan<sup>[5]</sup> with a modification to incorporate particle fragmentation (described below). The kinetics scheme for the model is based on superimposed cellulose, hemicellulose and lignin reactions.<sup>[5]</sup> In this manner, any biomass feedstock can be simulated through the knowledge of its initial mass composition with respect to these three primary components: Each of the virgin components undergoes the same generic competitive reaction scheme:



Throughout the paper, the term ‘tar’ is used to refer to the primary high molecular weight pyrolysis condensable sometimes called ‘bio-oil’ or ‘bio-crude’ and includes any enriched oxygen and water vapor content. The virgin components, ‘active’ intermediates and char are solid phase species, while tar and ‘gas’ are vapor products; all the species represent groups of compounds rather than pure chemical species. All reactions are modeled with first order Arrhenius kinetics. The frequency factors and activation energies for reactions  $K_1$ ,  $K_2$ ,  $K_3$ , and the mass ratio  $X$  are all dependent on the particular biomass component, whereas all heats of reaction and secondary tar decomposition parameters are independent of the source component. Reaction  $K_1$  has  $Ah_1 = 0$ , reaction  $K_2$  is endothermic with  $Ah_2 = 255 \text{ kJ/kg}$ , and both the char formation and secondary tar reactions are exothermic with  $Ah_3 = -20 \text{ kJ/kg}$  and  $Ah_4 = -42 \text{ kJ/kg}$ . All remaining parameter values are provided in Ref.<sup>[5]</sup>

The porous particle model incorporates all property variations, is valid both inside and outside the particle, and employs a fully transient momentum equation in contrast to the traditional use of the empirical Darcy’s Law. The derivation of the model has been addressed previously in Ref.<sup>[5]</sup> and only the final general form of the equations

is presented here. The governing equations for apparent densities ( $\rho$ ), gas velocity ( $u$ ), mass fraction of species  $\xi$  ( $Y_\xi$ ), total specific internal energy ( $e_t$ ) and the equation of **state** relating gas density, pressure ( $p$ ) and temperature ( $T$ ) are:

$$\frac{\partial \rho_{s,\xi}}{\partial t} = \dot{S}_{s,\xi}, \quad (5)$$

$$\frac{\partial \rho_g}{\partial t} + \frac{\partial}{\partial x_j} (\rho_g u_j) = \dot{S}_g, \quad (6)$$

$$\frac{\partial \rho_g Y_\xi}{\partial t} + \frac{\partial}{\partial x_j} (\rho_g Y_\xi u_j - \rho_g D_{eff}^{(\xi)} \frac{\partial Y_\xi}{\partial x_j}) = \dot{S}_{g,\xi}, \quad (7)$$

$$\frac{\partial \rho_g u}{\partial t} + \epsilon \left[ \frac{\partial}{\partial x_j} (\rho_g u_i u_j) \right] = -\frac{\partial p}{\partial x_i} + \frac{\partial}{\partial x_j} \left[ \mu_{eff} \left( \frac{\partial u_i}{\partial x_j} + \frac{\partial u_j}{\partial x_i} - \frac{2}{3} \frac{\partial u_j}{\partial x_j} \delta_{ij} \right) \right], \quad (8)$$

$$\frac{\partial e_t}{\partial t} + \frac{\partial}{\partial x_j} [e_g u_j - \lambda_{ij}^{eff} \frac{\partial T}{\partial x_i}] = p \frac{\partial u_j}{\partial x_j} + \sum \dot{S}_\xi \Delta h_\xi, \quad (9)$$

$$p = \frac{\rho_g}{\epsilon} \left( \sum Y_\xi / M_\xi \right) \bar{R} T, \quad (10)$$

where

$$\rho_g = \epsilon \hat{\rho}_g, \quad \rho_{s,\xi} = (1 - \epsilon) \hat{\rho}_{s,\xi}, \quad \epsilon = 1 - \sum \rho_{s,\xi} / \hat{\rho}_{s,\xi}, \quad (11)$$

$$D_{eff}^{(\xi)} = \epsilon D^{(\xi)}, \quad \mu_{eff} = \epsilon \sum Y_\xi \mu^{(\xi)}, \quad (12)$$

$$\lambda_{ij}^{eff} = (1 - \epsilon) \left\{ \frac{\sum \rho_\xi \lambda_{ij}^{(\xi)}}{\sum \rho_\xi} + \frac{\sigma d T^3}{\omega} \delta_{ij} \right\} + \epsilon \sum Y_\xi \lambda_{ij}^{(\xi)}, \quad (13)$$

and

$$e_g = \rho_g \left( \sum C_{vv}^{(\xi)} \right) T, \quad e_s = \left( \sum \rho_{s,\xi} C^{(\xi)} \right) T, \quad e_t = e_g + e_s, \quad (14)$$

where indices  $i, j$  correspond to coordinate directions (Einstein summation notation),  $\xi$  denotes species  $\xi$  (no summation over Greek indices) and  $\delta_{ij}$  is the **Kronecker** delta fiction. In the above formulation, subscripts  $s$ ,  $g$  and  $eff$  denote solid **phase**, gaseous phase and effective property values, respectively. Source terms due to reactions are represented by  $\dot{S}$ , the porosity is  $\epsilon$ , the molecular weight is  $M$ , the true density is  $\hat{\rho}$ , the universal gas constant is  $\bar{R}$  and summations are over all species of indicated phase. Additionally,  $\sigma$  is the **Stefan Boltzmann constant**,  $\omega$  is the biomass **emissivity** and  $d$  is a characteristic pore dimension; constant volume and solid phase

heat capacities are  $C_v$  and  $C$ , and **properties**  $\mu, D, \lambda$  are the viscosity, species **diffusivity** and thermal conductivity (tensor), respectively.

In addition to the momentum equation (8), it is convenient for multi-dimensional simulations to also consider the more traditional **Darcy's** Law which is valid only within the particle. **Darcy's** Law states that the velocity is proportional to the local pressure gradient and the permeability ( $\Gamma$ ):

$$u_i = -\frac{\Gamma_{ij}}{\mu_g} \frac{\partial p}{\partial x_j}, \quad (15)$$

where  $\mu_g$  is the gas viscosity. Both forms of momentum equations are investigated in the following section for the purpose of comparing **1D** and 2D Cartesian **geometry** simulation results. Several property values and initial conditions (subscript O) used for biomass woods are given in Table 1 while remaining **properties** are provided in **Ref.**<sup>[5]</sup> The models for both the pyrolysis kinetics and porous particle transport have been tested extensively by Miller and **Bellan**<sup>[5]</sup> and shown to agree well with a large number of experimental results from a variety of investigators. Note that in the above set of equations both the thermal conductivity and the permeability are presented in **full** tensor format in order to account for spatial variations as addressed below.

Boundary conditions **are** defined based on the geometry under consideration **and** the particular choice of momentum equation as explained below. **Particle** shapes are assumed to be parallelepipeds based on elongated wood 'splinters.' These shapes have been observed in **cold** flow visualizations in the bench scale vortex reactor at the National Renewable Energy Laboratory (**NREL**) (e.g. **Diebold** and **Power**<sup>[11]</sup>). Throughout the present work only **Cartesian** geometries are considered for both **1D** and 2D particle analyses. Boundary conditions on the wall side of the particle are independent of the momentum equation: the temperature at the solid surface is matched to the wall condition ( $T' = T_w$ ), the velocity is set to zero, and **all** other fluxes are **nulled** (zero first derivative). **Darcy's** Law being valid only within the particle, the model domain extends only to the outer edge of the particle; thus, the thermal boundary condition in direction  $i$  is based on a modeled surface condition (see e.g. **Di Blasi**<sup>[6]</sup>):

$$-\lambda_{n_j}^{eff} \frac{\partial T}{\partial x_j} = \sigma (T^4 - T_\infty^4) + h'(T - T_\infty), \quad (16)$$

where  $n$  is the coordinate direction normal to the surface. **Eq.(16) states that the heat flux entering the particle** is due to both radiative **and** convective exchange with the far field temperature  $T_\infty$ . In the present **work**, the **coefficient** of convection is assumed to be constant with  $h' = 20W/K$ . **The** pressure is assumed constant and equal to the **far** field condition. **With the** momentum **equation** derived from first principles (Miller and **Bellan**<sup>[7]</sup>), the solution domain includes regions outside of the particle, thereby accounting for the effects of exothermic tar reactions within the mass boundary layer immediately adjacent to the particle. Then, **boundary** conditions are provided by directly matching temperature and pressure values to the flow conditions at the particle location ( $T = T^*, p = p^*$ , where the superscript indicates local flow values), while velocity conditions **are** calculated through mass conservation constraints, and mass fractions are assumed to have **zero** first derivatives at the boundary. The use of both momentum equations and the **dimensionality** of the simulations are considered in the following section.

## 2.2 Turbulent Carrier Gas Model

**The** present vortex reactor is characterized by strongly swirling and recirculating flow regions. Such flows are poorly modeled using  $k - \epsilon$  and all other turbulence models which invoke the gradient **diffusion** hypothesis relating turbulent viscosity and mean strain **rate**. For complex flows of the type addressed here, full Reynolds stress closures are **recommended**<sup>[8]</sup> in which modeled transport equations are solved for each of the individual components of the Reynolds stress tensor. **The** particular **model** chosen for this work is the **fully** compressible (to account for strong density variations) single species model of **Zha** and **Knight**<sup>[9]</sup> with a modified model for the stress component **diffusion** terms (based on **Ref.**<sup>[10]</sup>). Furthermore, the model has been extended to include species transport and chemical reaction. The **tensorial** form of the final model for the transport of the ‘long time’ **Favre** averaged (density weighted) variables is:

$$\frac{\partial \bar{\rho}}{\partial t} + \frac{\partial}{\partial x_j} (\bar{\rho} \tilde{u}_j) = 0, \quad (17)$$

$$\frac{\partial \bar{\rho} \tilde{u}_i}{\partial t} + \frac{\partial}{\partial x_j} (\bar{\rho} \tilde{u}_i \tilde{u}_j) = -\frac{\partial \bar{p}}{\partial x_i} + \frac{\partial}{\partial x_j} (\bar{\tau}_{ij} - \overline{\rho u_i'' u_j''}) + \bar{\rho} g_i, \quad (18)$$

$$\frac{\partial \bar{\rho} \tilde{\epsilon}}{\partial t} + \frac{\partial}{\partial x_j} (\bar{\rho} \tilde{\epsilon} + \bar{p}) \tilde{u}_j = \frac{\partial}{\partial x_j} \left[ (\lambda + C_p \bar{\rho} C_h \frac{k^2}{\epsilon}) \frac{\partial \bar{T}}{\partial x_j} + \tilde{u}_i \bar{\tau}_{ij} - \overline{\rho u_i'' u_j''} \tilde{u}_i \right] + \sum \dot{S}_\xi \Delta h_\xi, \quad (19)$$

$$\frac{\partial \bar{\rho} \tilde{Y}_\xi}{\partial t} + \frac{\partial}{\partial x_j} (\bar{\rho} \tilde{u}_j \tilde{Y}_\xi) = \frac{\partial}{\partial x_j} \left[ \bar{\rho} (D + C_h \frac{k^2}{\epsilon}) \frac{\partial \tilde{Y}_\xi}{\partial x_j} \right] + \dot{S}_\xi, \quad (20)$$

$$\frac{\partial}{\partial t} (\overline{\rho u_i'' u_j''}) + \frac{\partial}{\partial x_k} (\overline{\rho u_i'' u_j''} \tilde{u}_k) = A_{ij} + B_{ij} + C_{ij} + D_{ij}, \quad (21)$$

$$\frac{\partial \bar{\rho} \epsilon}{\partial t} + \frac{\partial}{\partial x_j} (\bar{\rho} \epsilon \tilde{u}_j) = -C_{\epsilon,1} \frac{\epsilon}{k} \overline{\rho u_i'' u_j''} \frac{\partial \tilde{u}_i}{\partial x_j} - C_{\epsilon,2} \bar{\rho} \frac{\epsilon^2}{k} + \frac{\partial}{\partial x_j} \left[ (\mu + C_{\epsilon,3} \frac{k^2}{\epsilon}) \frac{\partial \epsilon}{\partial x_j} \right], \quad (22)$$

$$\bar{p} = \bar{\rho} \left( \sum \bar{R} \tilde{Y}_\xi / M_\xi \right) \bar{T}, \quad (23)$$

where the shear stress tensor is,

$$\tau_{ij} = \mu \left[ \left( \frac{\partial \tilde{u}_i}{\partial x_j} + \frac{\partial \tilde{u}_j}{\partial x_i} \right) - \frac{2}{3} \frac{\partial \tilde{u}_k}{\partial x_k} \delta_{ij} \right], \quad (24)$$

the kinetic and internal energies are,

$$k = \frac{1}{2} \overline{\rho u_k'' u_k''} / \bar{\rho}, \quad \tilde{\epsilon} = C_v \bar{T} + \frac{1}{2} \tilde{u}_k \tilde{u}_k + k, \quad (25)$$

and the Reynolds stress **production**, **diffusion**, pressure rate of strain and dissipation term models are:

$$A_{ij} = -\overline{\rho u_j'' u_k''} \frac{\partial \tilde{u}_i}{\partial x_k} - \overline{\rho u_j'' u_k''} \frac{\partial \tilde{u}_j}{\partial x_k}, \quad (26)$$

$$B_{ij} = \frac{\partial}{\partial x_k} \left[ \frac{C_s k}{\bar{\rho} \epsilon} \overline{\rho u_k'' u_l''} \frac{\partial}{\partial x_l} (\overline{\rho u_i'' u_j''}) \right], \quad (27)$$

$$C_{ij} = -C_{p,1} \frac{\epsilon}{k} \left[ \overline{\rho u_i'' u_j''} - \frac{2}{3} \bar{\rho} k \delta_{ij} \right] + C_{p,2} \bar{\rho} k \left( \frac{\partial \tilde{u}_i}{\partial x_j} + \frac{\partial \tilde{u}_j}{\partial x_i} \right), \quad (28)$$

$$D_{ij} = -\frac{2}{3} \bar{\rho} \epsilon \delta_{ij}, \quad (29)$$

respectively. In the above equations, subscripts  $i, j, k, l$  take values corresponding to the three orthogonal coordinate directions, the tilde is used to denote **Favre** averages and the double prime superscripts represent fluctuations with respect to the **Favre** average. In addition,  $C_p$  is the heat capacity at constant pressure,  $\mathbf{g}_i$  is the gravitational acceleration vector,  $\epsilon$  is the turbulence dissipation,  $\overline{\rho u_i'' u_j''}$  is the symmetric Reynolds stress tensor with six independent components, the subscript  $\xi$  corresponds to the gas phase species (steam, tar and gas); all remaining variables have been defined previously and properties are taken to be those of steam. Fluctuation



contributions to the reaction terms are neglected due to the first order nature of the reactions and the **relatively** small heats of **combustion** involved. **The** turbulence model constants **are** provided in Table 2.

Since the **full** three dimensional solution of **Eqs.(17)-(29)**is prohibitively expensive, it is assumed that the vortex reactor flow (see Fig. 1) is nearly **axisymmetric**, **the** assumption being valid when azimuthal variations are small compared to changes in the axial and radial directions; i.e.  $\partial/\partial\theta \ll \partial/\partial x, \partial/\partial r$ . *This* assumption is commonly used in confined swirling flow simulations (e.g. **Refs.**<sup>[8][11][12][13]</sup>), its validity being ensured within a short distance downstream of the entrance pipe. The ‘reduced’ equations are derived by expanding **Eqs.( 17)-(29)** into three dimensional cylindrical polar form and then dropping all terms involving derivatives with respect to the  $\theta$  direction (while retaining the azimuthal velocity). This results in a set of 15 coupled transport equations along with the equation of state which are integrated to steady state from ‘best guess’ initial conditions. The integration uses a second order accurate in space and time explicit McCormack finite difference scheme. Inflow conditions are generally obtained from experimental measurements and will be discussed in more detail below, whereas outflow conditions are specified through zero first derivative approximations for **all** variables except the axial velocity component which is found through mass conservation constraints. **Boundary** conditions along solid walls are based on a combination of wall fictions (following **Sharif and Wong**<sup>[11]</sup>) used to treat the turbulent boundary layer, constant outer wall temperature and zero first derivatives for remaining variables. Furthermore, the two **end walls at  $x = 0$ , and at  $x = L_r$**  are assumed to be thermally insulating for reasons to be discussed below. Boundary conditions at the outer wall (where the particles reside) are used to couple the turbulent flow equations to the remaining sub-models in a manner described below. **The** code has been rigorously tested and validated both through agreement between results of our simulation with the data from measurements of a confined swirling jet flow, and through comparison with the Reynolds stress model simulation of **Nikjooy and Mongia**<sup>[14]</sup> (isothermal and incompressible) that used **well** documented initial and downstream conditions. Comparisons showed good agreement between the current code and the cited results (not shown).

### 2.3 Particle Trajectory Model

The cold flow **visualizations** of **Diebold** and **Power**<sup>[1]</sup> suggest **that the** majority of wood particles in the vortex reactor remain in flat contact **with the wall, are parallelepiped in shape and in general** convect with major axis (along the grain) parallel to the flow direction. **This level of organization of the** particulate is less **likely** in the cone reactor design in which there are no grooves cut into the **chamber** surface for particle guidance. In the present model, the particles are assumed to remain **in** sliding contact with **the** wall. **In** addition, it is assumed that the particle's **relative** dimension in the transverse direction is **constant** and equal to the particle height normal to the wall,  $H_p$ . Therefore, the particle dimensions are specified by the choice of the height and the aspect *ratio*  $\Theta = L_p/H_p$  (where  $L_p$  is the particle length parallel to the grain). Lacking a complete resolution of the flow field around a real three dimensional wood particle, including the wake region, it is reasonable to assume that the drag experienced by the particle can be modeled **as** that over an elongated (prolate) spheroid having the minor axis equal **to**  $H_p$  **and** the same aspect ratio. Under **these** assumptions, **the trajectory** of a **single particle** is governed by both drag resulting from slip velocities with the exterior flow and by a friction force at the wall which impedes forward acceleration. The modeled equations for position and velocity (in the  $x$  direction along the outer wall) are:

$$\frac{dx_p}{dt} = u_p, \quad (30)$$

$$\frac{du_p}{dt} = f \left[ \frac{18V_p\mu}{m_p H_p^2} \right] (\tilde{u}_x^* - u_p) - f_\mu \frac{(\tilde{u}_\theta^*)^2}{R_R}, \quad (31)$$

where  $x_p$  and  $u_p$  are the instantaneous particle position and velocity,  $V_p$  and  $m_p$  are *the* particle volume and mass,  $f_\mu$  is the coefficient of sliding friction (assumed constant and equal to 0.1),  $g$  is the gravitational acceleration, the superscript  $*$  denotes carrier gas variables evaluated at the particle location, and the modeled coefficient  $f$  is:

$$f = 1 + \frac{3\Delta Re_p}{16} + \frac{9\Delta^2 Re_p^2}{160} \ln(\Theta Re_p/2), \quad (32)$$

where,

$$Re_p = \frac{\bar{\rho}^* |\tilde{u}_x^* - u_p| H_p}{\mu}, \quad (33)$$

and

$$A = \frac{8(0^2 - 1)/6}{\left[ (2\Theta^2 - 1) \ln(\Theta + \sqrt{\Theta^2 - 1}) / \sqrt{\Theta^2 - 1} \right] - @} \quad (34)$$

The bracketed term in [31] corresponds to Stokes drag over a **sphere**, whereas the factor **f** includes corrections for prolate spheroid aspect ratio at moderate particle Reynolds numbers (**Clift et al.**<sup>[15]</sup>). *The above equation set is Lagrangian and requires the specification of initial conditions for the particle position and velocity, in addition to the exterior turbulence flow field  $(\bar{\rho}^*, \tilde{u}_x^*, \tilde{u}_\theta^*)$  evaluated at the particle location  $(r = RR - 0.5 \text{ HP})$  as indicated by the superscript **\*** (**Favre** fluctuations neglected).*

### 3 SINGLE PARTICLE RESULTS

**Before** discussing the coupling of the individual sub-models, it is necessary to first analyze the behavior of the single stationary particle model and seek possible simplifications. **This** section is devoted to such analysis and includes discussions of the numerical solution procedure and range of parameters for the model, along with **further useful** evaluations. In particular, although the particle model has been derived in general tensor coordinates, **full** multidimensional simulations are prohibitively intensive **computationally**. A comparison of **1D** and 2D simulation results is made in this section in order to **quantify** the **conditions** under which the **1D** approximation is justifiable. The extent of individual particle response to external flow conditions is then investigated in order to simply the outer edge particle boundary conditions as described below. Finally, a new fragmentation model is introduced in order to describe physical breakup processes which persist for ablative pyrolysis.

#### 3.1 *Multi-Dimensional Particle Evaluation*

In order to assess the effects of dimensioned and directional effects for wood particles, the particle equations (1)-(15) are solved numerically on both **1D** and 2D grids. Darcy's Law is used instead of the **full** momentum equation for several reasons. First, **Darcy's Law** is **computationally** less intensive than the **full** momentum equation (8) due to both the numerical treatment of the pressure solution, and also because the domain extends only to the edges of the particle, thus requiring fewer computational grid points than the full equation solution which extends to

exterior regions. Second, the **full** momentum equation was developed for 1 D solutions applied to relatively large permeability porous **particles**; as such, it does not explicitly **include the** effects of varying **parallel** and cross grain permeability. Miller and **Bellan**<sup>[7]</sup> showed **that the** use of **Darcy's** Law **can result in substantial** over predictions of the **surface** temperature and pyrolysis rate. **Therefore**, it **will** be desirable to use **the full** equation for the **final** reactor calculations. However, for the present purposes of directional analysis, Darcy's Law is sufficient.

The numerical solution to the particle equations uses finite difference approximations to the governing equations. The solution procedure is essentially the same as applied in Miller and **Bellan**<sup>[7]</sup> with the exception that Darcy's Law is combined with the continuity equation to provide an equation for pressure in order to filter acoustic waves while retaining density variations. The resulting Poisson type equation is:

$$\frac{\partial}{\partial x_j} \left( \frac{\rho_g}{\mu_g} \Gamma_{ji} \frac{\partial p}{\partial x_i} \right) = - \left( \dot{S}_g - \frac{\partial \rho_g}{\partial t} \right). \quad (35)$$

Directional effects for both the permeability and the thermal conductivity of the wood are considered; however, mixed directional property variations are not considered, *i.e.*  $\Gamma_{ij} = \lambda_{ij} = 0$ , when  $i \neq j$ . Equation (35) is solved **through a** Jacobi iteration procedure at each numerical time step

The geometry for the particle simulations is that of an elongated rectangular particle in flat contact with a hot constant temperate wall. Coordinates for the rectangular particle are defined with  $x_1$  parallel to both the grain and the wall) and  $x_2$  in the normal direction (the wall is then located at  $X_2 = 0$ ). Calculations are made with identical particle size in the  $x_2$  direction,  $HP = 5mm$ , and 24 numerical grid points **are** used to **partition** the  $x_2$  dimension, with equal grid spacing used for the parallel grain dimension ( $L_p = \Theta H_p$ ). The single particle is assumed to be stationary in initially quiescent vapor phase steam. The symmetry in the  $x_1$  direction at the particle mid-point allows for the solution of only one half the entire domain. Values for the wood conductivity and permeability **are** also fixed in this direction as listed in Table 1 and correspond to approximate cross grain values for typical Maple wood (**SERI**<sup>[16]</sup>); the results for **all** ID simulations correspond to these cross grain property values. The kinetics scheme used for Maple wood follows the method of Miller and **Bellan**<sup>[5]</sup> by prescribing initial cellulose, **hemicellulose** and **lignin** content. **The** particle, wall and **free** stream temperatures are initially

uniform at  $400K$  and the pressure is  $p = 100kPa$ . During each simulation, the **wall and free** stream temperatures are both raised over a **duration** of  $30s$  from  $400K$  to their **final** values of  $T_w = T_\infty = 900K$ . The linear heating of the **surface** conditions is **necessary** for **numerical resolution** and does not **affect the value** of the **results** because the mass loss relative to the particle's **initial mass** is **always**  $< 10\%$  **at the final heatup time**. **All** simulations discussed in this section are terminated when **90%** of the virgin wood mass is consumed. For comparison, an entire 2D calculation utilizing  $24 \times 24$  numerical grid points ( $0 = 2$ ) requires approximately 6300s of central processor time on a Cray **J90 supercomputer** whereas the corresponding 1D simulation requires approximately 300s.

An example of directional property effects in a 2D particle simulation is illustrated in **Fig.2**. The figure depicts instantaneous velocity vectors for the internal flow field for three different simulations of particles with aspect ratio  $\Theta = 2$ . The wall is located at the surface  $x_2 = 0$  and the surface at  $x_1 = 0$  is a plane of **symmetry** located at the actual center of the particle. In all cases, the vector snap shots are taken at a time corresponding to **40%** reduction in the wood mass (virgin plus active). Particle initial conditions and properties are identical for all these simulations including  $\lambda_{11} = \lambda_{22} = \lambda$ , except the permeability which is varied in the parallel **grain** direction ( $\Gamma_{11}$ ). In general wood samples, the permeability in the parallel grain direction can exceed the cross grain permeability by several orders of magnitude (**SERI**<sup>[16]</sup>). The present results correspond to cases in which  $\Gamma_{11}/\Gamma_{22} = 1, 10, \text{ and } 100$ , for parts (a), (b) and (c) of the figure, respectively. **The** vectors suggest that tar and gas produced by pyrolysis exit all surfaces of the particle nearly uniformly when there are no preferential permeability effects (**Fig.2a**). However, when the permeability is increased parallel to the wood grain, the exiting gas flow is redirected nearly completely through the **surfaces** defined by  $x_1 = \pm H_p$ .

The preferential permeability effects illustrated in **Fig.2** can be quantified by examining the relative mass of tar collected from the particle as a function of time:

$$\beta = \frac{1}{m_{p,0}} \int_0^t \oint_A \rho_g Y_{tar} \vec{u} \cdot \vec{dA} dt, \quad (36)$$

where  $m_{p,0}$  is the initial particle mass and the inner integral is over **all** surfaces. Tar collection for single

isolated spherical biomass particles has been examined by Miller and Bellan<sup>[17]</sup> who studied the effects of reactor temperature, tar quenching and parameter sensitivity. **The mass** of **gas**, or **the** combined masses could also be examined; however, it is **the tar** which is **ultimately** of **interest** for **the present** purposes (in particular for hydrogen production), Figure 3 shows the **temporal evolution** of  $\beta$  for **each** of **the three 2D** simulations in **Fig.2**. Results from a **1D** simulation are also included for comparison. **The simulations** suggest that there is virtually no deviation in the temporal mass loss due to preferential permeability effects. **Only** a very small increase in conversion time, with negligible change in final tar collection, is observed as the parallel grain permeability is increased by two orders of magnitude. This result is similar to a previous observation made by Di Blasi<sup>[6]</sup> who found nearly no change in final char masses upon altering both the char and wood **permeabilities** in **1D** simulations using **Darcy's Law**. **The 1D** particle approximation is observed to slightly over predict conversion times and under predict all of the 2D tar collection **results** for all times. However, the final magnitude of  $\beta$  is only slightly lower than the maximum observed value from the 2D calculations.

In order to highlight the effects, and limitations, of the **1D** approximation it is **instructive** to compare simulation results for various values of the particle aspect ratio. Figure 4 depicts the tar collection as a **function** of time for both **1D** and 2D simulations with particle aspect ratios of 1, 2 and 4. **The** simulation parameters are identical to those discussed above and both the permeability and the conductivity have constant uniform values in order to isolate geometric effects. The **1D** case corresponds by definition to an infinite aspect ratio particle; however, the results show that the approximation becomes reasonable for realistic finite aspect ratios. Again, results for the **1D** geometry produce conservative estimates for  $\beta$  at **all** times and **all** aspect ratios. **The** primary effect of particle **geometry** is observed in the total conversion time which decreases with decreasing aspect ratio. This effect is directly related to the surface area exposed to heating and pyrolysis relative to the total particle volume. On the other hand, the final values for  $\beta$  are much less influenced by the aspect ratio. In **fact**, the deviation in this value between the **1D** approximation and a square particle is less than 5% of the initial particle mass. For  $\Theta = 2$  this deviation is reduced to approximately **2.5%**.

Biomass wood samples **also** have directional variations in **thermal** conductivity: a review of the literature shows that the conductivity is **generally** larger in **the** cross **grain** direction for **both hard** and **soft** woods. For example, measured ratios of  $\lambda_{11}/\lambda_{22}$  for white pine, **oak** and balsa are approximately 0.75, 0.80 and 0.88, respectively (SERI<sup>[16]</sup>). These ratios are dramatically smaller in magnitude than those observed for permeability. The effects of these deviations are illustrated in **Fig.5** which shows  $\beta$  as a **function** of *time* for both the **1D** and 2D simulations with three conductivity ratios. **The** aspect ratio is fixed at  $\Theta = 2$  and  $\Gamma_{11}/\Gamma_{22} = 1$  in **all** cases in order to isolate conductivity effects. As with the permeability, only relatively small effects of conductivity are observed for either the conversion time or the final tar mass. The **1D** approximation again results **in** conservative estimates for tar production with time; however, the final tar conversion is **well** predicted. Further simulations were conducted with conductivity ratios as large as 10 (not shown) which resulted in very large deviations from the behavior exhibited in Fig.5. Although such ratios are unrealistically large, they explain the permeability and aspect **ratio** behavior discussed when examining **Figs.3** and 4. Both conductivity and aspect ratio affect pyrolysis in a direct manner, *i.e.* the particle heating rate is a direct function of the ability to heat large portions of the wood to pyrolysis temperatures. **The** majority of heat transfer into the particle occurs through conduction. As such, the conductivity plays a strong role in pyrolysis (even though realistic directional variations are relatively small as shown in **Fig.5**). The particle's aspect ratio also plays a strong role by dictating the surface to volume **ratio** of the particle which is exposed to heating. However, permeability primarily determines the path of the pyrolysis gaseous **products** upon being formed, resulting in only minor and secondary effects on the pyrolysis evolution even when large directional variations are present.

The above results suggest that the **1D** particle geometry represents a valid approximation to the more complex multidimensional pyrolysis behavior for relatively large aspect **ratio** particles; in particular it produces conservative estimates of both tar collection and conversion time. The validity is not significantly affected by directional variations in the permeability, or for realistic values of the thermal conductivity. The approximation can also **be** considered justified for **small** aspect ratios ( $\Theta \geq 1$ ) when only the final product yields are of interest. When the

time evolution of pyrolysis products is needed, the 1 D approximation results in over predictions of the conversion time. However, the deviations in total conversion time become negligible in the context of the **vortex** reactor due to a large number of passes (recycle loops) made by each **particle** through the reactor (discussed below), and the **1D** approximation will, therefore be **considered** hereinafter. Furthermore, **all** simulations discussed hereinafter utilize the **full** momentum equation (8) in order to resolve the **thermal and mass boundary** layers adjacent to the **particle surface**, and the computational domain is **extended to** include the range  $0 \leq x_2 \leq 1.5H_p$  for **all simulations using** a 32 grid point **discretization**. The value 1.5HP is somewhat arbitrary; however, it is sufficiently large to resolve the region adjacent to the particle, while being small enough to allow for accurate sampling when the temperature and pressure boundary conditions **are** later matched to the boundary layer flow conditions. **All** further simulations are continued until **99%** decomposition of the virgin wood is completed and with a thermal boundary condition heatup time equal to one second per millimeter thickness  $HP$  unless otherwise specified. Test cases comparing the results from single isolated **1D** particle simulations with identical conditions (i.e.  $0 \leq X_2 \leq H_p$ ) using the two momentum equations reveal essentially identical evolutions (not shown).

### 3.2 Direct-Contact Particle Heating

To **further** the discussions of isolated particle simulations, it is **useful** to analyze the **efficiency of direct-contact** particle pyrolysis. This is accomplished by **performing** two **1D** simulations under the conditions previously discussed, i.e.  $H_p = 5mm$ ,  $T_w = 900K$ ,  $\bar{T}^* = 900K$ , where  $\bar{T}^*$  now corresponds to the local exterior flow **temperature** condition at  $x_2 = 1.5 HP$ . In the first simulation, heating is only performed at the wall while the thermal flux is null in the free stream. The opposite conditions are employed for the second simulation; in this case heating is exclusively from the free stream and the wall is insulating. Both the **tar** collection and mass averaged particle temperature,

$$\langle T \rangle = \frac{\int_0^{H_p} \rho'_s T \cdot dx_2}{\int_0^{H_p} \rho'_s \cdot dx_2} \quad (37)$$

evolutions are presented in Fig.6. The superscript  $'$  in the above equation denotes that solid phase char is **excluded**.<sup>[7][5][17]</sup> Clearly, the direct-contact wall heating provides a dramatically improved pyrolysis and heating



rates as **compared** to the flow heating case. The total conversion time is decreased by approximately 65% by direct-contact conduction heat transfer. For **free** stream heating, although thermal transfer occurs both through convection and conduction, **the thermal** conductivity of **the** gases is **nearly an** order of magnitude smaller than for the solid phases. Mass averaged heating **rates are** observed **to be as large as**  $\sim 10K/s$  for the wall heating case and can exceed the calculated values by **small** percentages for realistic multi-dimensional particles. Furthermore, larger heat transfer rates result in higher effective pyrolysis temperatures which yield significantly larger final tar collection values from direct conduction pyrolysis. These results suggest that direct-contact reactors offer a significant potential for improvement in pyrolysis yields for tar production when compared to non-contact and partial contact (**fluidized** bed) reactors.

### 3.3 *Particle Response to Carrier Gas Now*

**The** governing equations for an individual particle's trajectory (30)-(34) are **Lagrangian** and solved numerically through **forward** time differences. **These** equations describe both the position and velocity of each biomass test **particle** as it convects through the reactor. In **general**, a particle will make many passes through the reactor during its lifetime due to the recycle loop. As such, boundary conditions on the flow side of the particle ( $\bar{p}^*$ ,  $\bar{T}^*$ ,  $\bar{p}^*$ ,  $\tilde{u}_x^*$ ,  $\tilde{u}_\theta^*$  at  $x_2 = 1.5H_p$ ) **are** functions of the particle position, and hence of time. In addition, each recycle loop corresponds to a discontinuity in these boundary conditions as the particle is reset to  $x_p = 0$ , resulting in a difficult numerical resolution. In this section, we describe the conditions under which the time **average** values of the boundary conditions (denoted by the double brackets  $\langle\langle \rangle\rangle$ ) can be used instead of the complete time signal:

$$\langle\langle \phi^* \rangle\rangle = \int_0^{t_c} \phi^*(t') \cdot dt', \quad (38)$$

for any boundary condition variable  $\phi^*$ .

An analysis of the relative time scales is **useful** in predicting the particle response to the boundary conditions. The majority of heat **transfer** to the **particle** from the **free** stream occurs through thermal diffusion (convective heat transfer is away from the particle due to the venting of pyrolysis gases). **The** ratio of the time scale for

then-m1 diffusion ( $t_\lambda \sim \rho C H_p^2 / \lambda$ ) through the gas to the particle residence time during one loop through the reactor ( $t_R \sim L_R / \tilde{u}_{x,in}$ ) is:

$$\frac{t_\lambda}{t_R} = \frac{\rho C / \lambda}{L_R / \tilde{u}_{x,in}} H_p^2, \quad (39)$$

where  $\tilde{u}_{x,in}$  is the **particle** injection velocity into the reactor. In order to consider the particle pyrolysis evolution independent of **temporal** oscillations (and **therefore** well modeled using average boundary values), this ratio must be significantly larger than unity ( $t_\lambda \gg t_R$ ); i.e. *the particle* passes through the domain much faster than the thermal **diffusion** response time. Using properties for wood and an assumed injection velocity  $\tilde{u}_{x,in} = 10 \text{ m/s}$  with  $L_R = 1 \text{ m}$  suggests that particles with  $HP$  larger than approximately  $0.3 \text{ mm}$  ( $t_\lambda / t_r \approx 10$ ) can be justifiably assumed to respond only to average values for **free** stream boundary conditions.

To further illustrate the influence of boundary condition temporal oscillations on the **particle**, we calculate the particle response to a specified temporal disturbance in the free stream temperature boundary condition. his calculation is performed for a  $1 \text{ mm}$  particle using a boundary **temperature** equal to  $\bar{T}^* = 850 + 25 \sin(\omega' t)$ . The amplitude of  $\pm 25 \text{ K}$  is approximately the root mean square fluctuation calculated from actual reactor simulation results (not shown) and  $T_w = 900 \text{ K}$ . The temporal evolutions of tar collection produced from such simulations are presented in **Fig.7** for various values of the oscillation frequency. The value  $\omega' t = 0$  corresponds to no temperature fluctuations (*i.e.* using  $\langle \bar{T}^* \rangle$ ), while  $\omega' t_c = 30$  results in 30 periods and cm-responds approximately to the maximum number of **re-entrainment** loops for an experimental vortex reactor as estimated in **Ref.[1]** As it is clearly **observed**, there is no effect on pyrolysis due to thermal disturbances. The physical reason for this behavior is provided through the graphical illustration of char apparent density profile evolution displayed in **Fig.8** for the  $u' t_c = 0$  particle. The figure shows that even though there is a high temperature free stream boundary condition at  $X_2 = 1.5 H_p$ , the direct conduction heat transfer **from** the  $900 \text{ K}$  wall located at  $X_2 = 0$  is significantly stronger. The char profiles reveal that the pyrolysis occurs almost entirely on the wall side which results in a pyrolysis wave moving outward, towards the free stream, Only a small **fraction** of the pyrolysis occurs on the free stream side as indicated by a small bulge in the char profiles near  $X_2 = H_p$  for intermediate times. These

results suggest that time averaged values for free stream temperature and pressure boundary conditions result in no loss of information, as the pyrolysis is effectively decoupled *from the free stream* disturbances. In addition, these results provide **further justification** for **the use** of a **particle pyrolysis** model **with** quiescent adjacent flow (neglected cross flow), since effects from **the flow** side of **the particle** are minimal. **This** can be understood by considering that a co-flow can **affect the tar** collection (36) in one of **two** primary manners: 1) by changing the pyrolysis evolution and hence the mass of tar production, or 2) by affecting the ejection velocity at the particle **surface** ( $u_2$  only, for **1D simulations**). The above discussions have already highlighted how the thermal pyrolysis evolution is controlled primarily by the wall conditions; hence co-flow effects on pyrolysis are negligible. In addition, there is a velocity boundary layer due to no slip conditions such that  $u_1 \rightarrow 0$  at the particle surface. This indicates that the ejection velocity is determined primarily by the internal particle pyrolysis, and the co-flow can only dictate the direction of the pyrolysis gases upon exiting the particle, not the tar collection **parameter,  $\beta$** . Therefore, a quiescent particle model can be used for the present flow with no significant loss of **information**.

### 3.4 *Particle fragmentation*

The single particle model was originally derived to describe the pyrolysis of large stationary biomass particles in initially quiescent steam or nitrogen environments and under controlled experimental conditions. In the case of **stationary** direct surface **contact**, the particle is in direct thermal contact with a hot surface and heat transfer to the **particle** proceeds almost entirely from the contact edge of the **particle**. As the pyrolysis wave progresses, an insulating layer of char is **left** behind which substantially diminishes the **effective** heating **rate**.<sup>[7]</sup> **In contrast**, heating rates and conversion times are much **more** rapid in real reactors where the biomass particles convect at high velocities and pressures along the heated surface. Although no experimental measurements of such conversion times and pyrolysis yields are known to the authors, **Esteban Chomet**<sup>[18]</sup> of NREL suggests that large **particles ( $\sim 1\text{cm}$ )** have pyrolysis conversion times of  $\sim 1\text{s}$  for reactor wall temperatures of **900K**. This value is approximately two orders of magnitude smaller than for stationary particles of similar sizes and at similar temperatures and under the above mentioned conditions (see e.g. **Figs.3-6**). This large difference in conversion

times must be **reconciled** by **identifying** the pertinent physical causes which are unique to ablation pyrolysis.

One yet unproved explanation for the increase in pyrolysis rates under ablative conditions that has received renewed attention recently by Lede *et. al.* <sup>[19]</sup> is based on **the** possible existence of a liquid intermediate pyrolysis product ('active' in **Eqs.** (1) and (2)). The explanation speculates that such an intermediate, which remains liquid at the high temperature reactor conditions, forms a thin lubricating and highly conductive layer between the biomass particle and the hot reactor wall, thus increasing heat transfer rates to the **particle**. This layer is stated to be of negligible influence for lower temperature TGA conditions but becomes significant at the higher temperatures associated with ablation processes. However, such an argument appears inconsistent with the results of many isothermal, non-ablative experiments at similar temperatures (with up to **1000 K/s** heating to final temperature) which have been well described without **liquid** layer effects by a model which also agrees with experimental results obtained in the TGA **regime**.<sup>[5]</sup> Furthermore, no direct observations have ever been made of such a liquid and its existence is hypothesized primarily on indirect evidence such as observed similarities between the pyrolysis and actual solid phase melting, whereby pyrolysis is restricted to a relatively narrow band of temperatures. In this section we provide supporting evidence that rejects the liquid layer postulate and also present a new and self-consistent explanation for increased ablative heating rates.

Within the present context, it is **useful** to address at least the following three considerations related to the existence of an intermediate liquid layer of the type described above: (1) **The** limited range of temperatures over which pyrolysis is **observed** to occur has already been well explained in terms of the endothermicity of biomass reactions by several **researchers**.<sup>[7][20]</sup> (2) A liquid layer inserted between the particle and hot wall, regardless of thickness, cannot decrease the conversion times for direct wall contact particle pyrolysis, **This is** due to the **fact** that it is the insulating char layer that is the limiting factor in heat transfer from the **wall** (see Table 1). (3) It is **well** understood that the production of char from a non-fluid state results in a 'non-graphitizing', disordered carbon (hard **carbon**)<sup>[21]</sup>, in contrast to the smoother fine scale structure that would be observed had the char been produced directly from a fluid intermediate. The actual chars produced through pyrolysis of cellulose and other

biomass stocks are indeed observed to be of the disordered (amorphous) carbon **form**.<sup>[21][22]</sup> Therefore, chars produced during biomass pyrolysis are direct products of solid phase media and are not produced from a **liquid** ‘active’ intermediate.

In light of the above arguments, the observed discrepancy in heating rates can only be attributed to a mechanical breakup of the insulating char region formed between the heated **wall** and the **un-pyrolyzed** particle matrix; *i.e.* as the particle slides along the wall, this char layer is ‘smashed’ or scraped off due to large shearing and stress forces. This is evidenced by the fact that the chars collected from the NREL reactor are powder size ( $\sim 50\mu m$ ) in contrast to the large ( $\sim 1cm$ ) input wood **chips**.<sup>[1]</sup> In order to model these breakup processes it is **useful** to consider past work in the field of particle fragmentation. Kerstein and Niksa<sup>[23]</sup> used the results of both deterministic and statistical models based on percolation theory (geometric theory of the connectedness of irregular objects) to describe the fragmentation of carbon chars undergoing combustion. In their model, a homogeneous and stationary sample fragments due to a loss of structural integrity when the porosity reaches  $\approx 0.7$ ; a value found to be in good agreement with experiments. For the present situation, we hypothesize that there exists a similar critical value of the biomass porosity at which fragmentation of the char occurs. When this critical porosity is reached, the particle collapses upon the insulating char layer, thus bringing the **un-pyrolyzed** portion of the particle closer to the wall and increasing the effective heating rate. Unfortunately, percolation theory cannot be directly applied to the current more complex problem as the critical porosity is expected to depend on many unknown factors including the biomass feed stock, the particle velocity and the contact pressure.

In order to illustrate the possible effects of such a critical porosity (denoted  $\epsilon_c$ ), a series of simulations of the porous biomass particle equations (**Eqs.(5)-(14)**) are performed incorporating a simple **model** for critical porosity effects. Fragmentation modeling is implemented by assuming that as the porosity reaches the specified critical value on the wall side of the particle, the particular location comes into direct thermal contact with the wall due to the removal of all **fragmented** chars. In practice this is accomplished by setting the **temperature** to be  $T = T_{wall}$  for **all**  $\epsilon \geq \epsilon_c$  within the wall side of the **particle**. This model has the additional feature that all **un-pyrolyzed**

mass in the region  $\epsilon \geq \epsilon_c$  continues to react at the wall temperature as though it had fragmented into many small (kinetically **controlled**) **pieces**, each piece remaining in **thermal** contact with the **wall**. Consider a single Maple particle of initial **thickness**  $H_p = 5mm$  and temperature  $T_0 = 450K$ , that is exposed at time  $t = 0$  to a heated wall located at  $x_2 = 0$  on one side and a high **temperature steam** having the same temperature on the opposite side. **The** outer boundary for the solution of **Eqs.(5)-(14)** is **located** at  $x_2 = 1.5H_p$  in order to accurately capture **all** mass and species boundary layer phenomena. **The** one dimensional domain is **discretized** using 48 grid points and the proceeding simulations require between approximately 600s and 7200s of processor time on a Cray J90 **supercomputer**. Additional details of the solution procedure and boundary conditions can be found in **Refs.[5][7][17]** **Figure 9** shows both the tar collection variable  $\beta$  and the 99%/0 conversion time ( $t_c$ ) as a function of the critical porosity and for various values of the wall temperature. Fragmentation is **observed** to result in substantial variations in tar collection and several orders of magnitude decreases in conversion times. As the critical porosity approaches the initial matrix porosity,  $\epsilon_0 = 0.67$ , the solutions approach the kinetic pyrolysis limits. Note that the maximal tar collections are consistent with the upper bounds measured for nearly kinetically controlled Maple particles by Scott *et. al.*<sup>[24]</sup> The wide range of values for the conversion time and tar collection are evidence of the model's robustness in portraying a broad degree of ablation without resorting to a hypothetical liquid layer. Currently, there are no available quantitative experimental measurements under related conditions to guide the choice of a specific value of  $\epsilon_c$ , or to determine its dependence and sensitivity to velocity and pressure. In the absence of such information, a constant value  $\epsilon_c = 0.75$  is selected in order to match **suggested**<sup>[18]</sup> values of  $t_c \sim 1s$  at  $T_{wall} \approx 900K$ . **This** value for  $\epsilon_c$  is used hereinafter throughout the paper.

## 4 REACTOR RESULTS

The above sets of governing equations for the particle pyrolysis, turbulent reactor flow and particle trajectories are coupled through appropriate conservation constraints in order to provide a complete description of the final reactor operation. Under steady state operation, the contribution of **all** injected biomass particles can be simulated

by obtaining numerical solutions for a single ‘test’ particle for each injected size class and each biomass type contained within the reactor feed. As each **test** particle convects along the reactor outer wall, its free stream boundary conditions for **temperature and pressure correspond to the same conditions** for the turbulent reactor flow field at a position corresponding to  $r = RR - 1.5H_p$  (averaged as in **Eq.(38)**). On the other hand, complementary boundary conditions for the turbulent reactor flow equations must account for the presence of particles through a mild ‘wall blowing’ (tar and gas evolving from the pyrolyzing particles) whereby an inward directed radial velocity component enters the reactor through the outer wall. **This** wall inflow has appropriate contributions for the tar and gas being generated by the pyrolysis of a **single** test particle multiplied by the **local** particle number density ( $N$  is the number of particles per unit wall area specific to each test particle group):

$$N = \frac{\dot{m}_{feed}}{m_{p,0} 2\pi R_R u_{p,in}}, \quad (40)$$

where  $\dot{m}_{feed}$  is the specified mass feed rate of **particles**, and  $u_{p,in}$  is the particle injection velocity. Such a coupling is valid as long as  $H_p \ll RR$ . It is assumed that the **local** number density  $N$  corresponding to each injected test particle remains constant throughout the particle’s evolution (divergence free spread velocity along the wall) and that the particles are in direct sliding contact with the wall and maintain a tight helical path through the reactor such that their downstream axial paths can be described by a continuous  $u_p(x)$  in the **axisymmetric** coordinates (see Fig. 1). **Re-entrainment** is performed by re-introducing **all** particles that reach the down stream edge of the reactor,  $z = L_R$ , and the tar and gas generated from each recycle loop, size class and biomass type are superimposed. The actual mass of flow entering the real recycle loop is assumed to be much smaller than that passing through the exit pipe. In this case, the recycle loop is not included in the reactor simulation as its practical implementation is of questionable validity due to the **axisymmetric** geometry. For conditions in which each test particle makes many passes through the reactor (satisfied in this work), the particle contributions are essentially equal to the total tar and gas yields from each test particle multiplied by the total number of particles within the reactor and then distributed uniformly over the entire outer wall surface area. This results in a near uniform value for  $\bar{\rho}\tilde{u}_r(r = R_R)$  corresponding to the rate of gaseous mass generation from **all** particles. **Boundary**

conditions for the tar and gas mass fractions at the reactor wall are derived to include the diffusion (molecular plus turbulent) velocity:

$$(\Psi_{\xi} \bar{\rho} \tilde{u}_r) |_{r=R_R} = (\tilde{Y}_{\xi} \bar{\rho} \tilde{u}_r) |_{r=R_R} - \left[ \bar{\rho} (D + C_h \frac{k^2}{\epsilon}) \frac{\partial \tilde{Y}_{\xi}}{\partial r} \right] |_{r=R_R}, \quad (41)$$

where  $\Psi_{\xi}$  is the relative fraction of the generated gaseous mass ( $\bar{\rho} \tilde{u}_r |_{r=R_R}$ ) for species  $\xi$ . Equation (41) ensures that the proper mass of tar and gas enter the domain: it is an implicit relation for the outer wall boundary conditions,  $\tilde{Y}_{\xi} |_{r=R_R}$ , and is solved at each numerical time step and axial wall node. In practice the test particle, trajectory and turbulent reactor flow equations are first solved independently using guessed coupling conditions and then successive iterations are performed until a converged steady state solution is obtained.

Simulation of the current NREL vortex reactor requires the specification of the reactor geometry, wall temperature and all pertinent inflow conditions; however, these parameters have not been documented (note that the reactor has been renovated since the publication of Ref.<sup>[1]</sup>) and these values must therefore be estimated. Table 3 contains a list of all ‘base case’ geometry and inflow conditions used hereinafter in the reactor simulations. The inflow profiles (i.e. at  $z = 0$ ) are uniform in the region  $R_R - D_{in} \leq r \leq R_R$  and slightly smoothed near the boundaries for numerical stability. The turbulent inflow is pure steam whose mean turbulence kinetic energy is assumed to be equally divided among each of the three diagonal components of the Reynolds stress tensor. However, the off-diagonal terms at the inflow have a zero first derivative allowing the development of a more natural measure of anisotropy. The radial injection velocity is null and the turbulence dissipation rate  $\epsilon$  is modeled using a commonly used function of  $k$  and the inflow pipe diameter,  $D_{in}$ .<sup>[14]</sup> In addition, an axial velocity component must be defined such that the correct mass flow rate ( $\rho \tilde{u}_{\theta, in} \pi (D_{in}/2)^2$ ) of steam entering the numerical domain is obtained. The axial velocity is calculated using the ratio of the true entrance pipe area to the numerical axisymmetric inflow area:

$$\tilde{u}_{z, in} = \tilde{u}_{\theta, in} \left[ \frac{\pi (D_{in}/2)^2}{\pi [R_R^2 - (R_R - D_{in})^2]} \right] = \tilde{u}_{\theta, in} \left[ \frac{1}{4} \left( \frac{\Phi_1}{2 - \Phi_1} \right) \right], \quad (42)$$

where  $\Phi_1 = D_{in}/R_R$ . Note that if the pipe diameter has its maximum value,  $D_{in} = R_R$ , then the inflow remains



predominantly swirling with  $\tilde{u}_{x,in} = 0.25 \tilde{u}_{\theta,in}$ . In addition, the injected particles are assumed to be in dynamic and thermal **equilibrium with the steam flow** (zero **slip and zero temperature** difference, i.e.  $u_{p,in} = \tilde{u}_{x,in}$  and  $T_{p,0} = \bar{T}_{in}$ , respectively). All reactor **flow** simulations **incorporate** a numerical grid having 192 x 48 grid points in the  $(x, r)$  plane and require approximately 7200s of processor time on a **Cray J90 supercomputer** for convergence to steady state mean reactor flow. Generally, two or three **iterations** between **the** test particle, particle trajectory and reactor flow equations are needed for final convergence.

Figure 10 depicts various steady state  $(z, r)$  reactor flow profiles of the steady state solution from the base case simulation with  $T_{wall} = 900K$  ( $r = 0$  is the axis of symmetry). The velocity vectors in Fig. 10a reveal a region of strongly recirculating **core** flow near the entrance region of the reactor as it is expected for strongly swirling confined flows (e.g. Refs.<sup>[12][13]</sup>). The temperature contours in Fig. 10b show that this recirculation zone consists primarily of low temperature material entrained from the inflow. However, further downstream the core flow is rapidly heated due to turbulent convective heat transfer from the walls. Had heated wall conditions been used for the end walls at  $x = 0$  and  $x = L_R$ , both the recirculation region and the reactor core temperature would be significantly larger than the current values. Such high temperate conditions would enhance tar decomposition (through **Eq.(4)**) within the reactor, thus decreasing its efficiency for tar collection from the exit pipe flow. **Tar** and gas mass fraction contours are presented in Figs. 10c and 10d, respectively. Although the mass addition of these species generated by the biomass pyrolysis is nearly uniform along the  $r = RR$  wall, the actual boundary condition values increase monotonically with  $x$  due to the effects of the turbulent diffusion term in **Eq.(4 1)**. However, for **all** axial locations, both the tar and **gas** profiles have maximal values at the wall and decrease monotonically towards the central reactor core region,

#### 4.1 Reactor **Efficiency** and Wall **Temperature Effects**

Regardless of the particulars of the interior reactor flow profiles, the ‘true’ measure of the reactor **efficiency** for tar production can be determined quantitatively by comparing the actual mass rate of tar exiting the reactor ( $\Omega_R$ )

and the mass rate of tar exiting the particles ( $\Omega_p$ ):

$$\Omega_R = \int_0^{0.5D_{out}} 2\pi r (\bar{\rho} \bar{Y}_{tar} \tilde{u}_x) |_{x=L_R} \cdot dr, \quad (43)$$

$$\Omega_p = \sum \left\{ 2\pi R_R N \int_0^{t_c} (\rho_g Y_{tar} u) |_{n=H_p} \cdot dt \right\}, \quad (44)$$

where the summation is over all particle size classes and biomass types (i.e. **all** different test particles injected).

**With** these definitions two unique measures of the reactor performance are the reactor efficiency ( $\eta$ ) and the % tar reduction ( $\gamma$ ):

$$\eta = \Omega_R / \dot{m}_{feed}, \quad \gamma = (\Omega_p - \Omega_R) / \Omega_p, \quad (45)$$

which **quantify** the relative efficiency of reactor tar production normalized by the mass feed rate of biomass and the relative proportion of tar produced in the reactor which is decomposed to gas before exiting the reactor, respectively.

A brief evaluation of the above relations and the following model aspects yields an interesting feature of the **reactor efficiency parameters**  $\eta$  and  $\gamma$ : (1) The results of **Figs.7** and 8 showed that the mass of tar produced by the particles ( $\Omega_p$ ) is dependent almost exclusively on the wall temperature due to the dominance of pyrolysis on the wall side of the particle **relative** to the flow side heating. (2) The species mass fraction equations (**Eq.(20)**) are linear in  $\bar{Y}_\xi$ . (3) The **exothermicity** of tar reactions is essentially negligible due to its relatively small heat of combustion and the very dilute fractions of tar observed (see Fig. 10c). (4) Under the assumptions of the model, any increase (decrease) in mass injection rate results in a corresponding linearly proportional increase (decrease) in the tar and gas mass fraction values along the outer wall due to particles. (5) **The** mass rate of generation of tar and gas by the particles is much smaller than the inflow pipe mass flow rate of steam, 'The ensemble characteristics lead to the following conclusion: both of the efficiency parameters  $\eta$  and  $\gamma$  are essentially independent of the biomass feed rate,  $\dot{m}_{feed}$ . In addition, considerations (2) and (3) indicate that for fixed reactor **geometry**, the parameter  $\gamma$  is essentially a function of the wall temperature only. These conclusions have been tested using actual results from a variety of simulations (not shown).

Figure 11 shows the steady **state** efficiency **parameters** for the base case reactor flow as a function of both the wall temperature and the corresponding minimum heating energy:

$$E_{\min} = \int_0^{L_R} 2\pi R_R [(\lambda + C_p \bar{\rho} C_h \frac{k^2}{\epsilon}) \frac{\partial \bar{T}}{\partial r}]_{r=R_R} \cdot dx + \dot{m}_{feed} C (T_{wall} - T_{p,0}), \quad (46)$$

which is given by the summation of the integrated thermal **flux rate** through the outer wall and the estimated energy needed to raise the particle mass feed from **its** initial temperature to the wall temperature. This minimum energy ax-responds to a perfectly insulating reactor with no heat loss to the surroundings, and both the steam and pyrolysis gases are assumed to be transparent to radiation heat transfer from the reactor walls. For the present conditions, the contribution **from** the second term on the right hand side of **Eq.(46)** due to particle heating is in all cases less than **5%** of the total  $E_{\min}$ ; therefore, the majority of input energy is used to heat the steam. Although  $E_{\min}$  could be reduced by increasing the inflow steam temperature, similar power would still be required for the necessary steam pm-heat. The results of Fig. 11 show an optimal wall temperature of approximately **900K** for which tar harvest is maximized at slightly more than 80°/0 of the feed mass. **The** vortex reactor is characterized by competing influences of& and  $\gamma$  which both increase linearly over the range of temperature considered. These two effects result in the optimal wall temperature observed which corresponds to a minimum input energy of approximately **355kW** required to heat both the steam carrier gas and the Maple particles.

#### **4.2 Particle Size, Biomass Type and Size Distribution**

Miller and **Bellan**<sup>[17]</sup> observed that relative tar yields are significantly increased as the initial particle size decreases. This effect was attributed to the relative residence time of tar within the particle and its adjacent boundary layer. The longer residence times associated with large particles allow for more substantial tar decomposition to gas through **Eq.(4)**. Using similar reasoning, tar yields are maximized for very small particles which approach the kinetic limits of pyrolysis (provided that tar can be rapidly quenched upon exiting the particle). However, these trends due to particle size are not observed in the present simulations as illustrated by Fig. 12 which shows the reactor efficiency as a **function** of wall temperature for the base case conditions and for two particle sizes. Note

that the curves are nearly identical for temperatures  $T_{wall} > 800K$ . This new behavior is due to the introduction of the critical porosity for fragmentation. As  $\epsilon_c \rightarrow \epsilon_0$  the pyrolysis occurs very rapidly and approaches the kinetic limits regardless of the initial particle size. All gaseous pyrolysis products are forced at increasingly large velocities out of the particle before significant decomposition can occur. **Therefore**, as  $\epsilon_c \rightarrow \epsilon_0$  the pyrolysis becomes independent of the initial particle size. For the present case of  $\epsilon_c = 0.75$ , the results show only negligible differences in behavior between  $H_p = 1mm$  and  $H_p = 5mm$  particles, except at very low wall temperatures. When  $T_{wall} < 800K$  the pyrolysis rate is relatively slow as compared to the tar reaction rate and the particle size becomes more significant.

Effects of different biomass **feedstocks** and **polydisperse** particle injection distributions can also be investigated with the model. Table 4 shows various steady state reactor efficiency values calculated for the base case conditions with the optimal  $T_{wall} = 900K$  together with the biomass contributions of cellulose, **hemicellulose** and **lignin**.<sup>[5]</sup> Tar harvest is observed to be strongly dependent on the **lignin** content of the biomass which is known to be the primary source of **char**.<sup>[5]</sup> In general, the representative **Bagasse** gross, Maple and Oak woods **all** result in very similar tar collections from the reactor due to **their similar compositions**. **It is only for the relatively extreme** samples of pure cellulose and high **lignin** content Olive Husk that large deviations in tar yield are observed.

Due to the primary influence of the wall heating on the particle pyrolysis and corresponding lack of **particle-flow** and particle-particle interactions, the model predicts that **polydisperse** particle injections will result in essentially mass weighted **linear** superpositions of the contributions from each individual test particle. Consider a **bimodal** injection of Maple particles with  $HP = 1mm$  (denoted group I) and **Olive** Husk particles with  $H_p = 5mm$  (denoted group II). In this case a **dispersity** variable ( $\alpha$ ) can be defined based on the relative injection rate of Maple particles:

$$\alpha = \frac{\dot{m}_{feed}(I)}{\dot{m}_{feed}(I) + \dot{m}_{feed}(II)} \quad (47)$$

which takes continuous values between 0 (pure group II) and 1 (pure group I). The superposition effect is illustrated for this **bimodal** distribution in Fig. 13. Therefore, within the range of conditions for which the current model is

applicable, results for any polydisperse mixture injection can be deduced through knowledge of the individual pure component/pure initial particle size behaviors.

#### 4.3 Reactor Scaling

As discussed above, the mass of tar produced by particles ( $\Omega_p$ ) can be optimized through appropriate choices of the reactor wall temperature and biomass species. The reactor configuration and inflow steam parameters therefore primarily affect only the relative decomposition of the tar once it exits the particles and proceeds through the reactor. In this section, the effects of the reactor geometry and scaling are investigated in order to suggest optimal conditions for minimizing tar conversion to gas within the reactor. A mathematical estimate for the extent of such reactions is obtained by examining the ratio of the tar residence time within the reactor ( $t_R \sim L_R/\tilde{u}_{x,in}$ ) relative to the characteristic time scale for tar decomposition ( $t_{tar} \sim K_{tar}^{-1}$ , where  $K_{tar}$  is the Arrhenius reaction rate from Eq.(4)):

$$\frac{t_R}{t_{tar}} \sim \left( \frac{L_R}{\tilde{u}_{x,in}} \right) K_{tar} = 16 \left[ \frac{R_R \Phi_2}{\tilde{u}_{\theta,in}} \left( \frac{1}{\Phi_1} - \frac{1}{2} \right) \right] \times \left[ A_{tar} \exp \left( \frac{-E_{tar}}{\bar{R}T_{wall}} \right) \right], \quad (48)$$

$$0 < \Phi_1 \leq 1, \quad \Phi_2 > 0, \quad (49)$$

where  $A_{tar} = 4.28 \times 10^6 s^{-1}$  is the tar reaction frequency constant,  $E_{tar} = 108 kJ/mol$  is the corresponding activation energy,  $\Phi_2 = LR/2RR$  is the overall reactor aspect ratio and Eq.(42) has been invoked. The first term in brackets on the right hand side of Eq.(48) is due to reactor geometry and inflow steam mass rate, whereas the second bracketed term is due entirely to the wall temperature. Note that the above estimate does not reveal any dependence on the exit pipe diameter as the tar residence time is primarily only dependent on the axial injection velocity and the reactor length. Optimal reduction of tar decomposition occurs when  $t_R/t_{tar} \ll 1$  in which case the tar is removed from the reactor much faster than it can react to form gas. Note that the use of  $T_{wall}$  as a characteristic reaction temperature results in generating an upper bound for  $t_R/t_{tar}$  as the majority of tar is located away from the walls where the temperature is in reality always less than  $T_{wall}$  (see Fig. 10b).

An evaluation of the above time scale ratio for the base case reactor parameters as a function of wall temperature

is depicted in Fig. 14 for three different reactor scales. The scale factor ( $M$ ) in this case represents a direct multiplication of the reactor length and radius by the particular  $M$  factor (e.g.  $M = 3$  is a reactor having  $L_R = 3m$  and  $R_R = 0.375m$ ); all **remaining dimensions and** parameters **are** determined by the relations in Table 3 and previous discussions. The time scales clearly illustrate how tar decomposition is increased with both increasing wall temperature (due to higher reaction rates) and increasing reactor scales (due to longer tar residence times). In fact, the curve for  $M = 1$  shows clearly that these reactions should become significant ( $t_R/t_{tar} \sim 0.1$ ) for **wall temperatures** of  $\approx 900K$ , which is also the optimal reactor temperature found previously from the simulation results of Fig. 11.

The accuracy of the time scale estimate,  $t_R/t_{tar}$ , in predicting reactor performance can be **further** confirmed by comparing the results of complete **simulations**. Figure 15 shows the reactor efficiency and  $\%_{tar}$  reduction parameters calculated **from** base case simulations with  $T_{wall} = 850K$  **as a function** of the reactor scale. The relative extent of tar decomposition reactions appears to increase linearly with  $M$  exactly as predicted by **Eq.(48)** which is linear in  $R_R$  (with  $\Phi_2$  fixed). A comparison of Figs. 14 and 15 along with the above discussions appears to indicate that ‘good’ reactor designs which minimize tar decomposition are characterized by  $t_R/t_{tar} < 0.1$ . This would indicate that a large reactor needs to operate at low temperatures. Unfortunately, low temperatures do not promote large tar **generation** from the particles indicating that large reactor sizes are **undesirable**.

## 5 CONCLUSIONS

A detailed mathematical model of vortex pyrolysis reactors used for harvesting tar from biomass has been presented, The model is based on detailed sub-models for the porous particle pyrolysis, **turbulent** reactor flow and test particle trajectories. The sub-models were chosen for their ability to capture the pertinent physics and were based on the **requirements** of each sub-system. The kinetics and porous particle model of Miller and **Bellan**<sup>[5]</sup> were chosen to simulate the individual particle pyrolysis. Both one dimensional ( **1D**) and two dimensional ( **2D**) Cartesian coordinate simulations were performed in order to assess the effects of geometry and spatial property

variations for single particles. **The** results showed that the 1 D model based on cross grain properties yields correct qualitative pyrolysis behavior while providing slightly conservative estimates for the quantitative particle conversion times. However, **the** total tar and gas products predicted by **the** 1 D approximation are in good agreement with the multidimensional simulations. Further results were obtained exclusively with the 1 D model. The **individual** particle **trajectories** were then modeled based on a prolate spheroid particle drag coefficient and on contact friction with the wall. Extensive studies of these equations showed that the individual **particle** pyrolysis evolution is effectively de-coupled from temporal disturbances of the temperature and pressure **boundary** conditions on the flow side of the particle. This means that the particle responds to only time averaged values of the flow properties, and greatly simplifies the solution procedure. A new fragmentation model was then introduced into the particle equations to account for mechanical breakup of the insulating char layers which occurs during ablative pyrolysis. Large ablative heating rates were shown to be well described by the fragmentation model without resorting to the artificial introduction of a liquid ‘active’ lubricating layer. In order to properly simulate the complex reactor flow, a compressible form of the **full** Reynolds stress transport model for swirling **axisymmetric** flow was used. **All sub-models were then coupled using appropriate conservation laws to provide complete solutions to the steady state vortex** reactor problem.

The simulation results elucidated many of the important physical processes and characteristics of the vortex reactor for tar collection from biomass pyrolysis. An optimal reactor wall temperature was identified as  $T_{wall} \approx 900K$  for which tar yields are maximized. This value was found to be practically independent of the initial particle size for *HP* as large as **5mm** due to relatively severe char fragmentation. It was additionally observed that tar yields can be increased by using low **lignin** content feed stocks, and that they are independent of the initial particle aspect ratio if the assumptions necessary for the one dimensional particle equation approximation are satisfied ( $\Theta \geq 2$ ). **Polydispersity** of the injected biomass was shown to be well modeled using mass weighted superpositions of the **pure substance/single** particle size distribution contributions. Under the base case reactor conditions with biomass injection having  $\dot{m}_{feed} = 50kg/hr$  of 5mm Maple particles and  $T_{wall} = 900K$ , it was

found that more than 80% of the mass feed **can be** harvested in **the form** of **tar**. his optimal case requires a minimum of **355kW** of operational input power **to heat both the carrier gas and the biomass**. Note that the tar yields measured in this work depend to a significant extent on the proper choice of the critical **porosity ( $\epsilon_c$ )** for the fragmentation model. **The** critical porosity was **only** estimated and **it is** recommended that experimental **measurements** should be performed to determine its value.

Evaluation of simulated results and a simple model indicate that the time scale ratio ( $t_R/t_{tar}$ ) is directly **proportional to the** reactor size (both its radius and **overall** aspect ratio). In **contrast**,  $t_R/t_{tar}$  is inversely proportional to both the entrance flow velocity and the entrance pipe diameter. Therefore, tar reactions within the reactor can be reduced by: (1) small reactors in both size and length to diameter ratio, (2) large steam inflow velocity and **mass flow rate**, (3) low reactor wall temperatures which reduce the tar reaction rate. Note that criteria (2) must be balanced with a corresponding increase in the energy needed to heat the inflow steam ( $E_{min}$ ) while (3) must be balanced with its adverse relation on the total tar produced by the biomass **particles**. It is therefore recommended that vortex reactors used to harvest tar from biomass pyrolysis operate with  $T_{wall} \approx 900K$  **with large** inflow **velocity and flow rate, and have relatively small length and aspect ratio similar to the base case geometry investigated here**. For commercial applications using large mass feed rates, we recommend the utilization of multiple small reactors operating in parallel rather than a single scaled up reactor.

## ACKNOWLEDGMENTS

This research was **conducted** at the Jet Propulsion Laboratory (**JPL**) and sponsored by the U.S. **Department** of Energy (DOE), with Mr. Neil **Rossmey** (DOE Headquarters) and **Mr. D. Hooker** (DOE Golden Center) serving as contract **monitors**, under an agreement with the National Aeronautics and Space **Administration**. Computational resources are provided by the super computing facility at JPL.



## REFERENCES

1. **J.P.Diebold** and A. Power, Engineering aspects of the vortex pyrolysis reactor to produce primary pyrolysis oil vapors for use in resins and adhesives. In A. V. **Bridgwater** and J. L. **Kuester**, editors, *Research in Thermochemical Biomass Conversion*, pages 609-628. **Elsevier** Applied Science, New York, New York, 1988.
2. E. **Chomet**, D. Wang, D. Montane, and S. **Czemik**. Hydrogen production by fast pyrolysis of biomass and catalytic steam reforming of pyrolysis oil. In **A.V.Bridgwater**, editor, *Advances in' Thermochemical Biomass Conversion*, volume 1, pages 246-262. **Blackie** Academic and Professional, New York, New York, 1994.
3. **B.M. Wagenaar**, J.A.M. **Kuipers**, W. **Prins**, and W.P.M. van **Swaaij**. The rotating cone flash pyrolysis reactor. In **A.V.Bridgwater**, editor, *Advances in Thermochemical Biomass Conversion*, volume 2, pages 1122-1133. **Blackie** Academic and Professional, New York, New York, 1994.
4. **G.V.C.Peacocke** and **A.V.Bridgwater**. Design of a novel ablative pyrolysis reactor, In **A.V.Bridgwater**, editor, *Advances in Thermochemical Biomass Conversion*, volume 2, pages 1134-1150. **Blackie** Academic and Professional, New York, New York, 1994,
5. **R.S.** Miller and J. **Bellan**. A generalized biomass pyrolysis model based on superimposed cellulose, **hemicellulose** and **lignin** kinetics. *Comb.Sci. Tech.*, 1997. *In Press*.
6. C. **Di Blasi**. Analysis of convection and secondary reaction effects **within** porous solid fuels undergoing pyrolysis. *Combust.Sci.and Tech.*, 90:3 15-340, 1993.
7. **R.S.** Miller and J. **Bellan**. Analysis of reaction products and conversion time in the pyrolysis of cellulose and wood particles. *Comb. Sci.Tech.*, 119:331-373, 1996.
8. **W.P.** Jones and A. **Pascau**. Calculation of confined swirling flows with a second order moment closure. *Trans. ASME*, 111:248-255, 1989.
9. **G. Zha** and D. Knight. **Three-dimensional shock/boundary-layer** interaction using **reynolds** stress equation turbulence model. *AIAA J.*, 34(7):1313-1320, 1996.
10. **B.E.** Launder, **G.J.Reece**, and W. Rodi. Progress in the development of a **reynolds-stress** turbulence closure. *J. Fluid Mech.*, 68(3):537-566, 1975.
11. **M.A.** Sharif and **Y.K.E.** Wong. Evaluation of the performance of three turbulence closure models in the prediction of confined swirling flows. *Comps.and Fluids*, 24(1):8 1-100, 1995.
12. **D.G.** Sloan, **P.J.** Smith, and **L.D.** Smoot. Modeling of swirl in turbulent flow systems. *Ping. Energy Comb. Sci.*, 12:163-250, 1986.
13. M. **Nallasamy**. Turbulence models and their applications to the prediction of internal flows: A review. *Comp.and Fluids*, 15(2): 151-194, 1987.

14. **M. Nikjooy** and **H.C. Mongia**. A second-order modeling study of **confined** swirling flow. *Int. J. Heat and Fluid Flow*, 12(1):12–19, 1991.
15. **R. Clift**, **J.R. Grace**, and **M.E. Weber**. *Bubbles, Drops and Particles*. Academic Press, New York, New York, 1978.
16. **SERI**. A survey of biomass gasification: **Volume ii** - principles of gasification. Technical **Report** TR-33-239, **Solar** Energy Research Institute, Golden, Colorado, July 1979.
17. **R.S. Miller** and **J. Bellan**. **Tar** yield and collection **from** the pyrolysis of huge biomass particles. *Comb. Sci. Tech*, 1997. In Press.
18. **E. Chomet**. Personal communication, 1997.
19. **L. Lede**, **J.P. Diebold**, **G.V.C. Peacocke**, and **J. Piskorz**. The nature and properties of intermediate and **unvaporized** biomass pyrolysis materials. In **A.V. Bridgwater** and **D.G.B. Boocock**, editors, *Developments in Thermochemical Biomass Conversion*, volume 1, pages 27-42. Blackie Academic and Professional, New York, New York, 1997.
20. **R Narayan** and **M.J. Antal**. Thermal lag, fusion, and the compensation effect during biomass pyrolysis. *Ind. Eng. Chem. Res.*, 35(5):1711-1721, 1996.
21. **E. Fitzer**, **K. Mueller**, and **W. Schaefer**. The chemistry of the pyrolytic conversion of organic compounds to carbon. In **M. Dekker**, editor, *The Chemistry and Physics of Carbon*, volume 7, pages 237-377. M. Dekker, New York, 1971.
22. **M.J. Wornat**, **R.H. Hurt**, **N.Y.C. Yang**, and **T.J. Headley**. Structure and compositional transformations of biomass chars during combustion. *Comb. and Flame*, 100(1):13 1–143, 1995.
23. **A.R. Kerstein** and **S. Niksa**. Fragmentation during carbon conversion: Predictions and measurements. In *20th Symposium (International) on Combustion*, pages 941-949. 1984.
24. **D.S. Scott**, **J. Piskorz**, **M.A. Bergougnou**, **R. Graham**, and **R.P. Overend**. The role of **temperature** in the fast pyrolysis of cellulose and wood. *Ind. Eng. Chem. Res.*, 27:8–15, 1988.

# TABLES

Property	Value
$\rho_{s,0}$	$650 \frac{kg}{m^3}$
$\epsilon_0$	0.67
$C_i$	$2.3 \frac{kJ}{kg \cdot K}$
$\lambda$	$1.256 \times 10^{-4} \frac{kJ}{m \cdot s \cdot K}$
$r$	0.05 <i>Darcys</i>
$\lambda_{char}$	$8.37 \times 10^{-5} \frac{kJ}{m \cdot s \cdot K}$

Table 1: Property and initial parameter values for wood (across grain) and char.

Constant	Value
$C_s$	0.22
$C_h$	0.0857
$C_{p,1}$	4.325
$C_{p,2}$	0.179
$C_{\epsilon,1}$	1.01
$C_{\epsilon,2}$	1.80
$C_{\epsilon,3}$	0.10

**Table 2:** Turbulence model constants.

Parameter	Value
$L_R$	$1.0m$
$RR$	$0.125m$
$D_{in}$	$0.4R_R$
$D_{out}$	$RR$
$\bar{T}_{in}$	$450K$
$\bar{p}_{in}$	$100kPa$
$\tilde{u}_\theta$	$200m/s$
$k$	$0.2\tilde{u}_\theta^2$
$\epsilon$	$k^{3/2}/0.4D_{in}$
$HP$	$5mm$
$e$	$2$
$\dot{m}_{feed}$	$50kg/hr$ Maple

Table 3: Base case reactor geometry and inflow conditions.

Biomass	Cellulose	Hemicellulose	Lignin	$\eta$
cellulose	1	0	0	<b>0.903</b>
<b>Bagasse</b>	0.36	0.47	0.17	0.824
Maple	0.40	0.38	0.22	0.814
oak	0.35	0.40	0.25	0.824
Olive husk	0.22	0.33	0.45	0.749

**Table 4:** Compositions and **reactor** efficiencies for base case conditions and various biomass with  $T_w = 900K$ .

## FIGURE CAPTIONS

Figure 1: Schematic of the vortex reactor.

Figure 2: Velocity vectors for a 2D wood **particle** with aspect ratio  $\Theta = 2$  ( $x_1 = 0$  is a plane of symmetry) at a time corresponding to 40% reduction of the virgin wood mass; (a)  $\Gamma_{11}/\Gamma_{22} = 1$ , (b)  $\Gamma_{11}/\Gamma_{22} = 10$ , (c)  $\Gamma_{11}/\Gamma_{22} = 100$ . The particle height is  $HP = 5mm$ , and the heating conditions are  $T_w = T_\infty = 900K$ .

Figure 3: Comparison of 1D and 2D particle pyrolysis simulation tar collections for various ratios of the parallel to cross grain permeability. **The particle** height is  $HP = 5mm$ , with  $\Theta = 2$ , and the heating conditions are  $T_w = T_\infty = 900K$ .

Figure 4: Comparison of 1D and 2D particle pyrolysis simulation tar collections for various particle aspect ratios. The particle height is  $HP = 5mm$ , and the heating conditions are;  $T_w = T_\infty = 900K$ .

Figure 5: Comparison of 1D and 2D **particle** pyrolysis simulation tar collections for various ratios of the parallel to cross grain thermal conductivity. The particle height is  $HP = 5mm$ , with  $\Theta = 2$ , and the heating conditions are  $T_w = T_\infty = 900K$ .

Figure 6: Comparison of (a) tar collections and (b) mass averaged particle temperature obtained through exclusive heating at either the wall or the flow boundary for 1D particle pyrolysis employing the complete momentum equation (**Eq.(8)**) with  $HP = 5mm$  and  $T_w, T^* = 900K$ .

Figure 7: Temporal evolution of the tar collection for a 1D particle simulation having  $T^* = 850 + 50 \sin(\omega' t)$ . **The** simulation conditions are  $HP = 1mm$  and  $T_w = 900K$ .

Figure 8: Temporal development of apparent char density profiles during a 1D particle simulation. **The** simulation conditions are  $HP = 1mm$ ,  $T_w = 900K$ ,  $\bar{T}^* = 850K$  and the profiles correspond to times;  $t/t_c = 0.25, 0.5, 0.75, 1.0$  and  $t_c = 12.9s$ .

Figure 9: Single particle pyrolysis behavior for **5mm Maple sample as a function of the critical porosity for fragmentation**; (a) tar collection, (b) 99% conversion time. **The** value  $\epsilon_c = \epsilon_0 = 0.67$  is the kinetic limit.

Figure 10: Steady state vectors and contours from a reactor simulation for base case conditions with  $T_{wall} = 900K$ ;

(a) velocity vectors, (b) temperature, (c) tar mass fraction x100, (d) gas mass fraction x100.

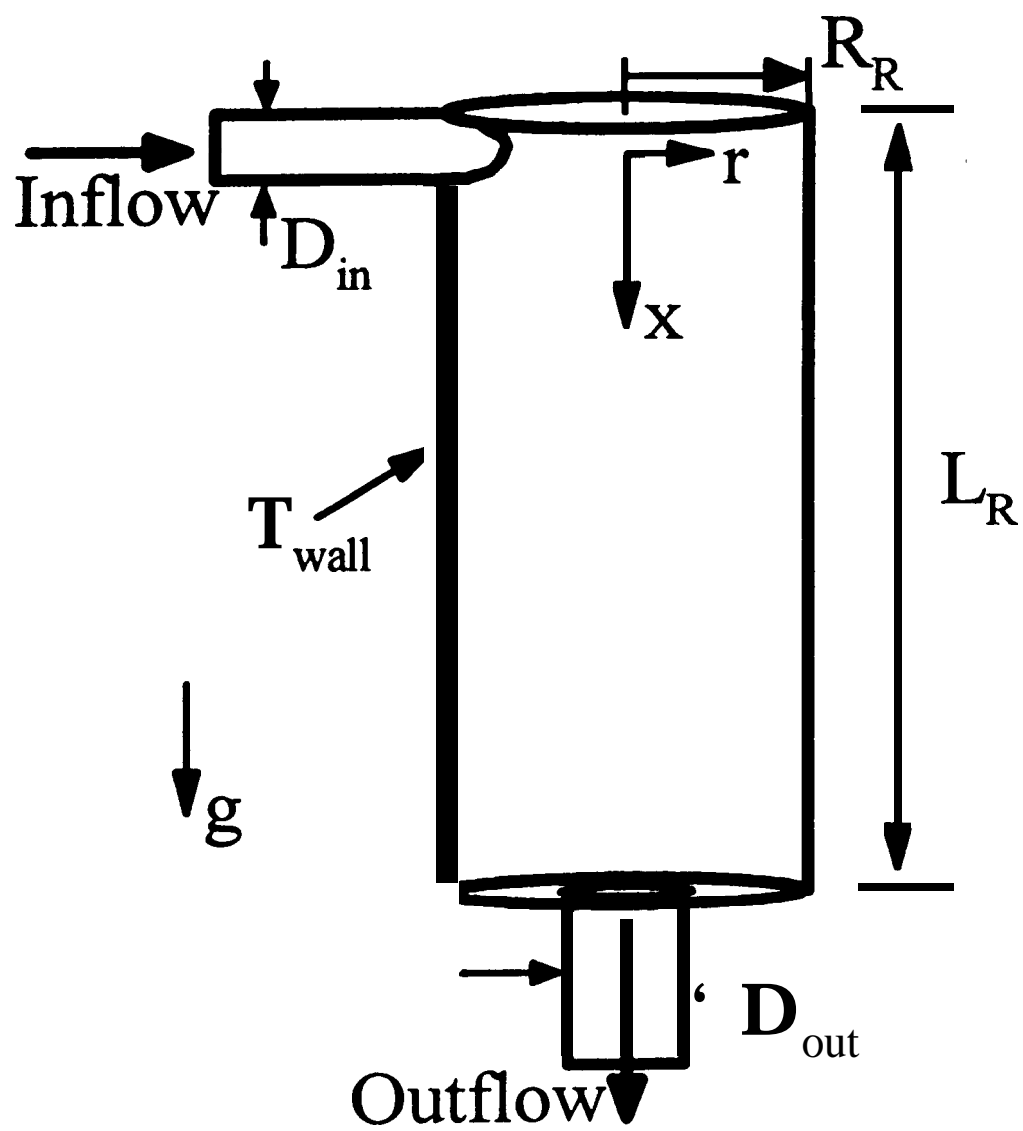
Figure 11: Reactor efficiency and %<sub>tar</sub> reduction for base case conditions as a **function** of (a) wall temperature and (b) minimum input energy.

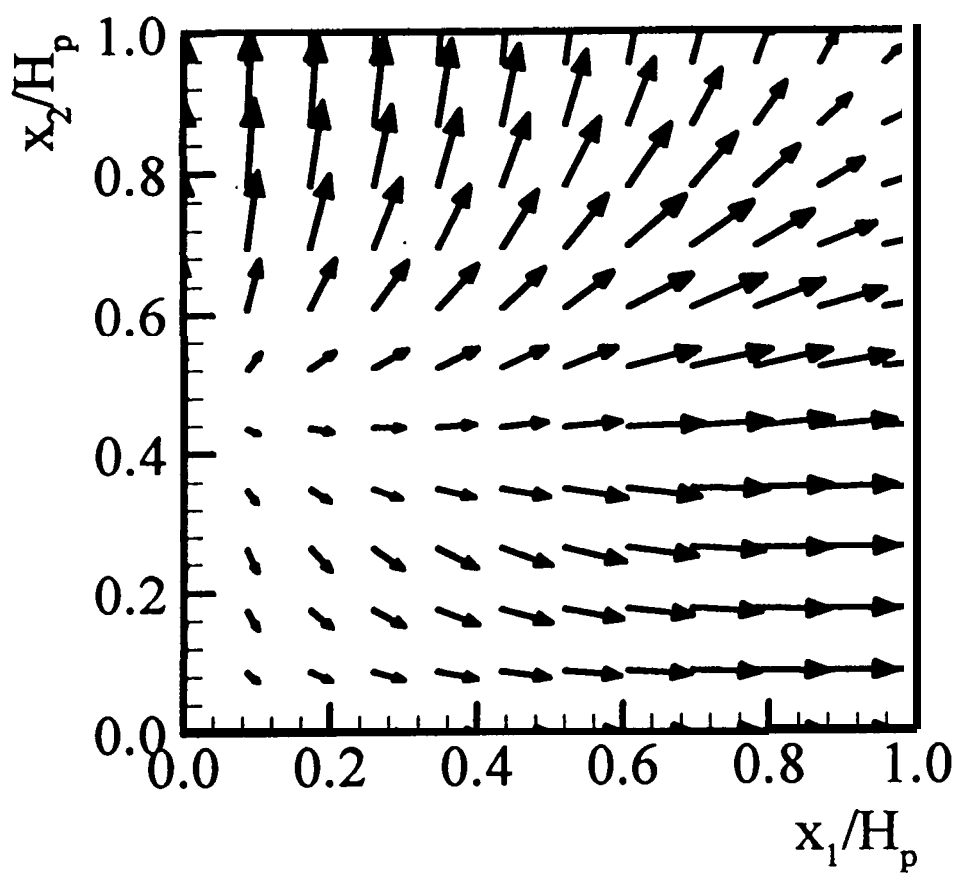
Figure 12: Reactor efficiency as a function of **wall** temperature for two initial particle sizes.

Figure 13: Reactor efficiency for base case conditions as a **function** of dispersity for biomass feed mixtures of **1mm** Maple and **5mm** Olive Husk particles.

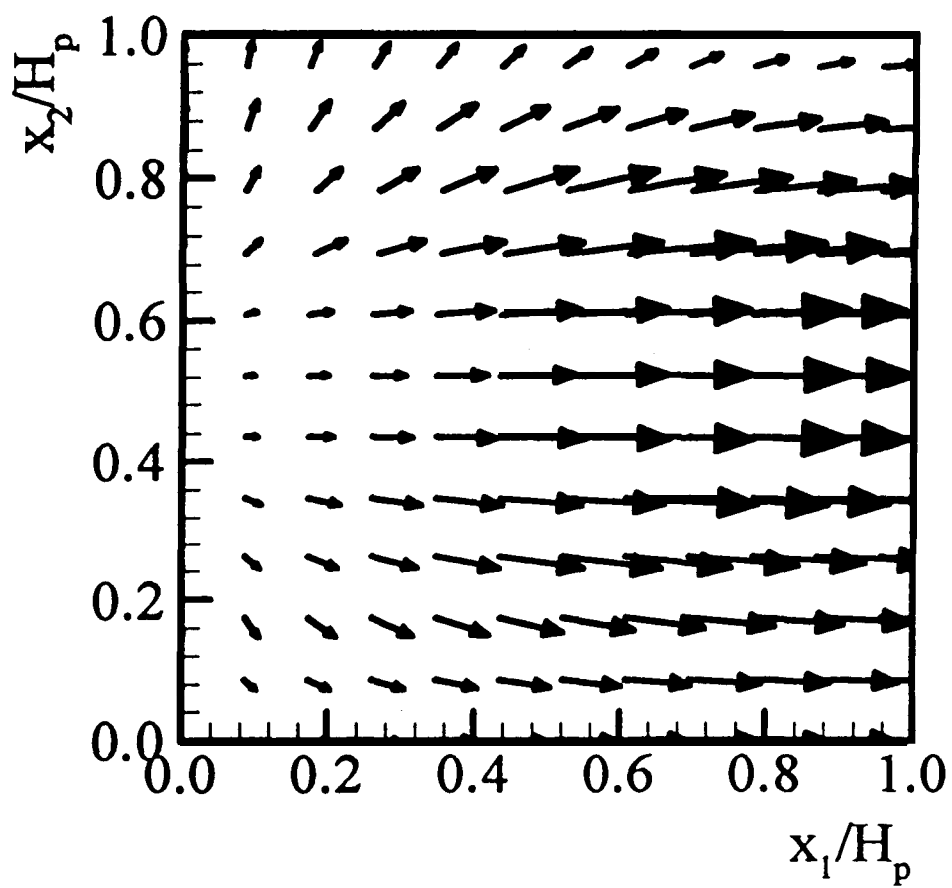
Figure 14: Ratio of reactor residence time scale to tar decomposition reaction time scale as a **function** wall **temperature** for various values of the reactor scale **factor** ( $M$ ).

Figure 15: Reactor efficiency and % tar **reduction** as a **function** of the reactor **scale factor** for base case conditions with  $T_{wall} = 850K$ .

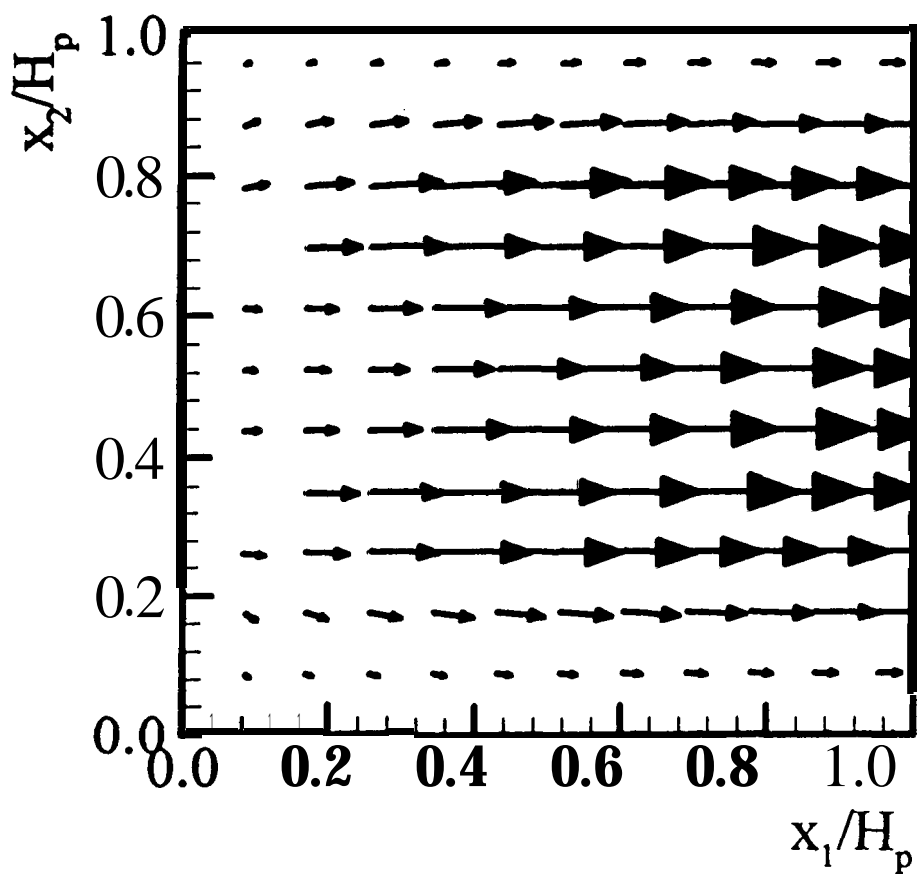




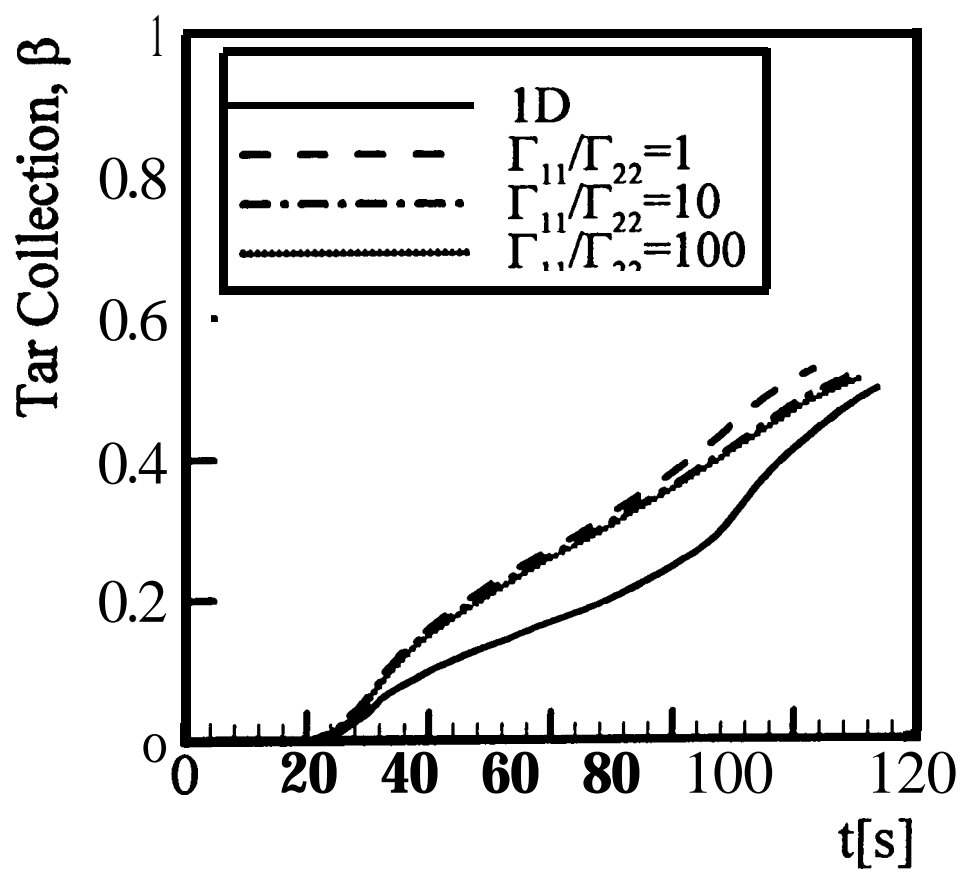


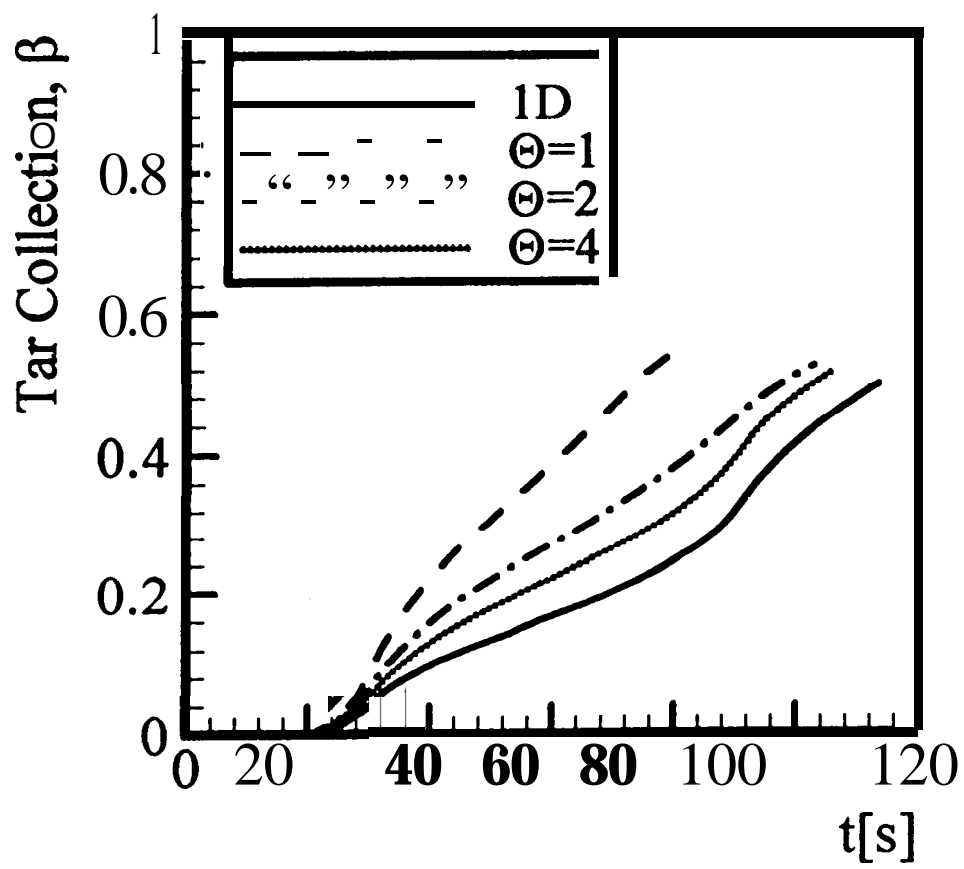


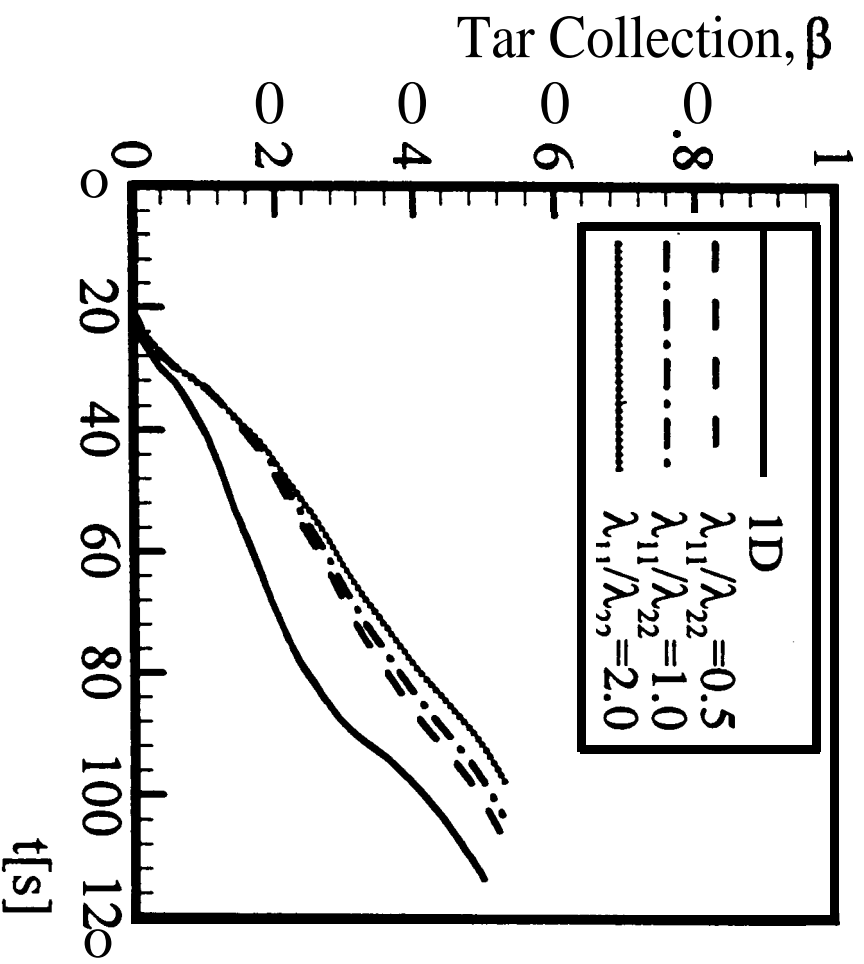
2b



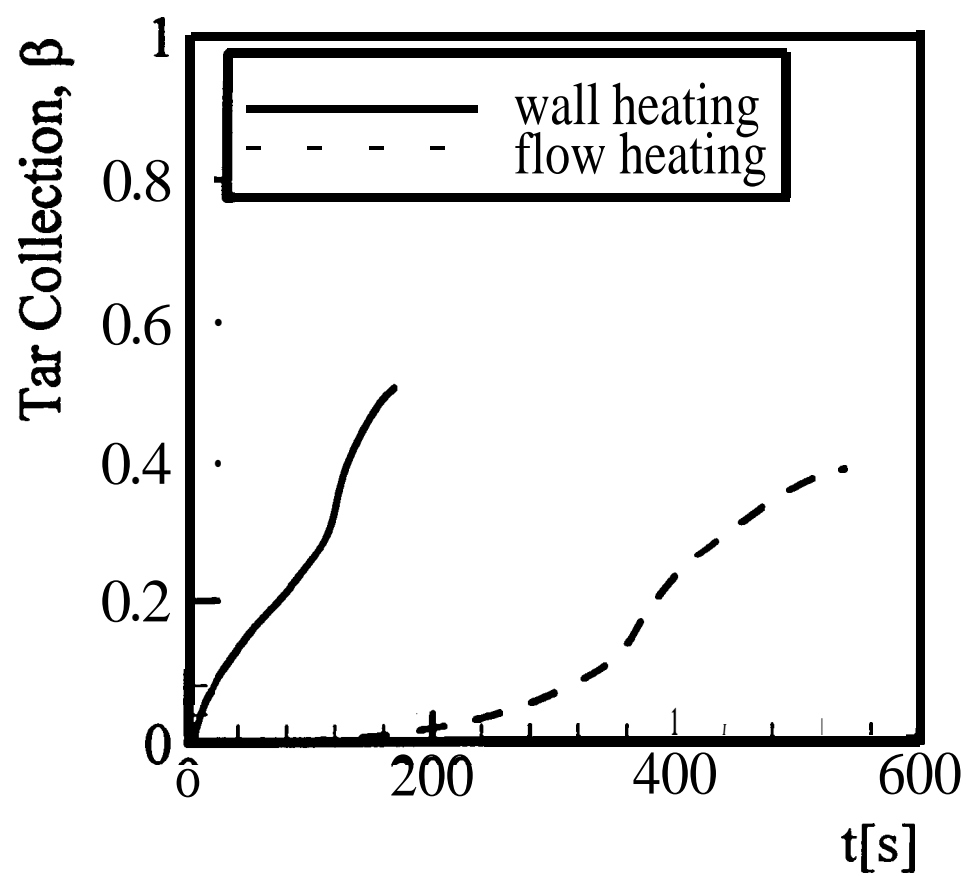
2c



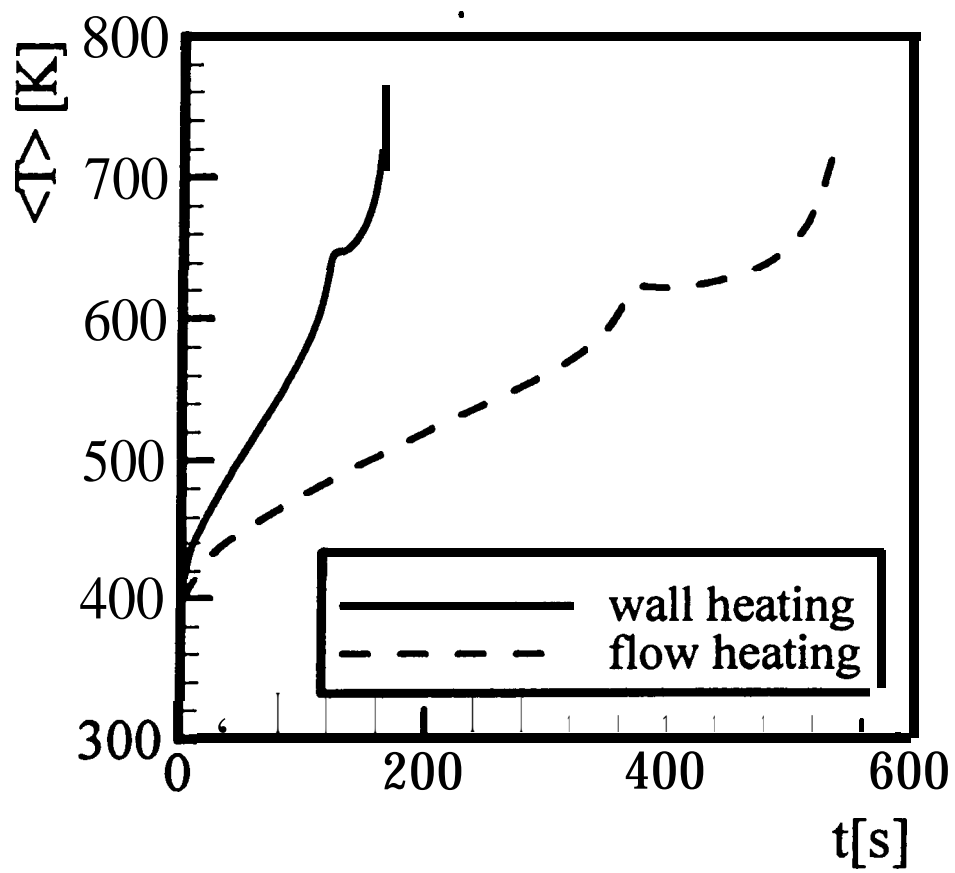


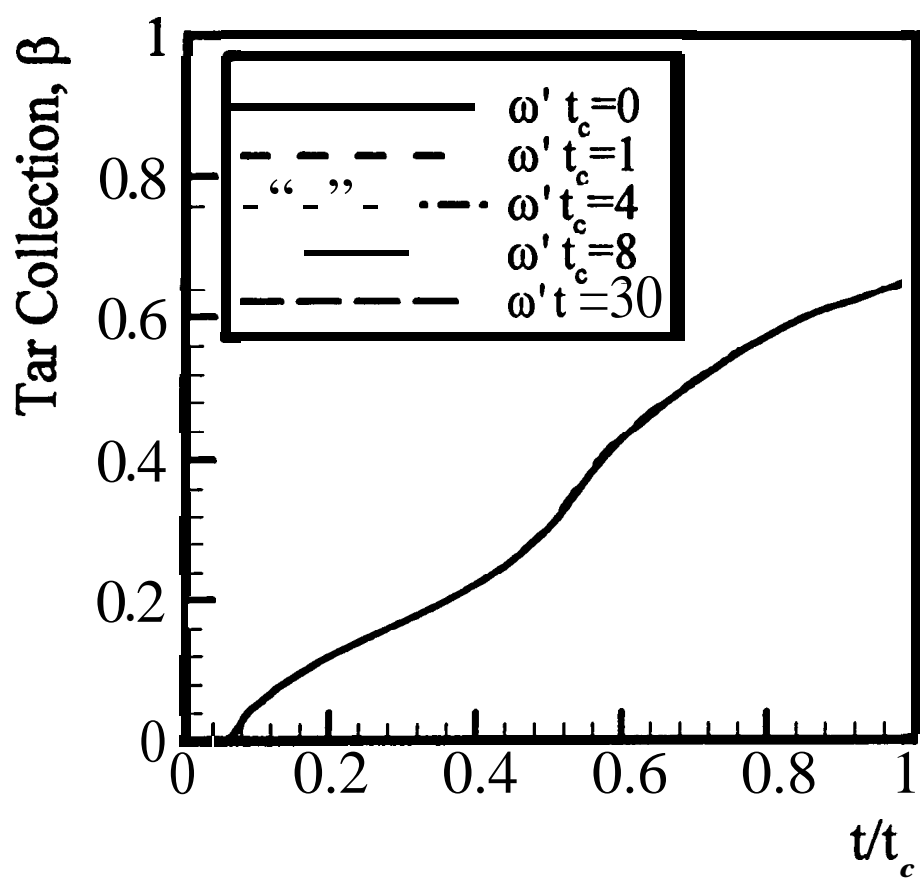


5



Ca

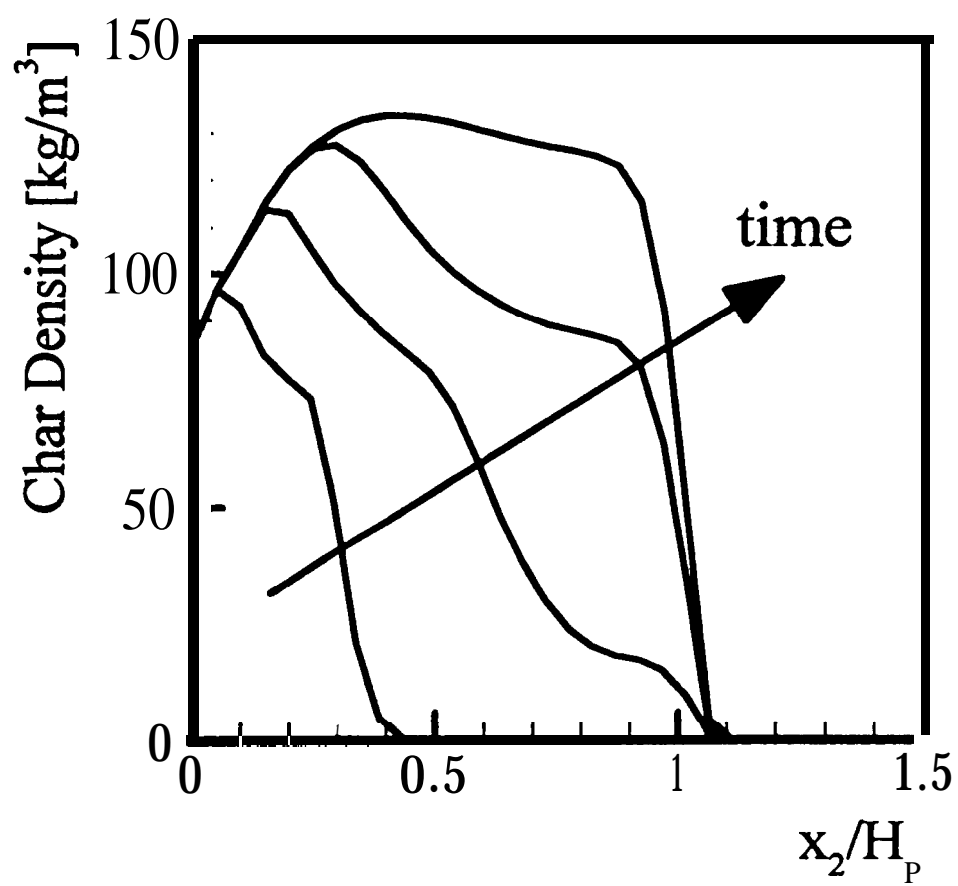


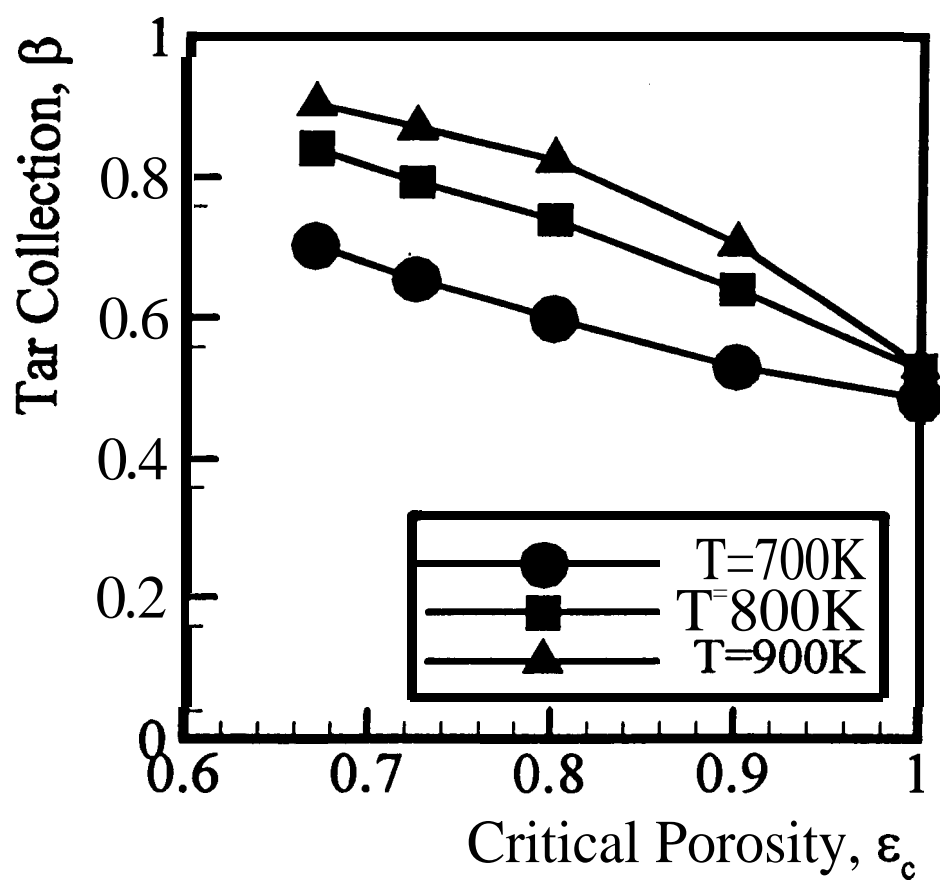


7

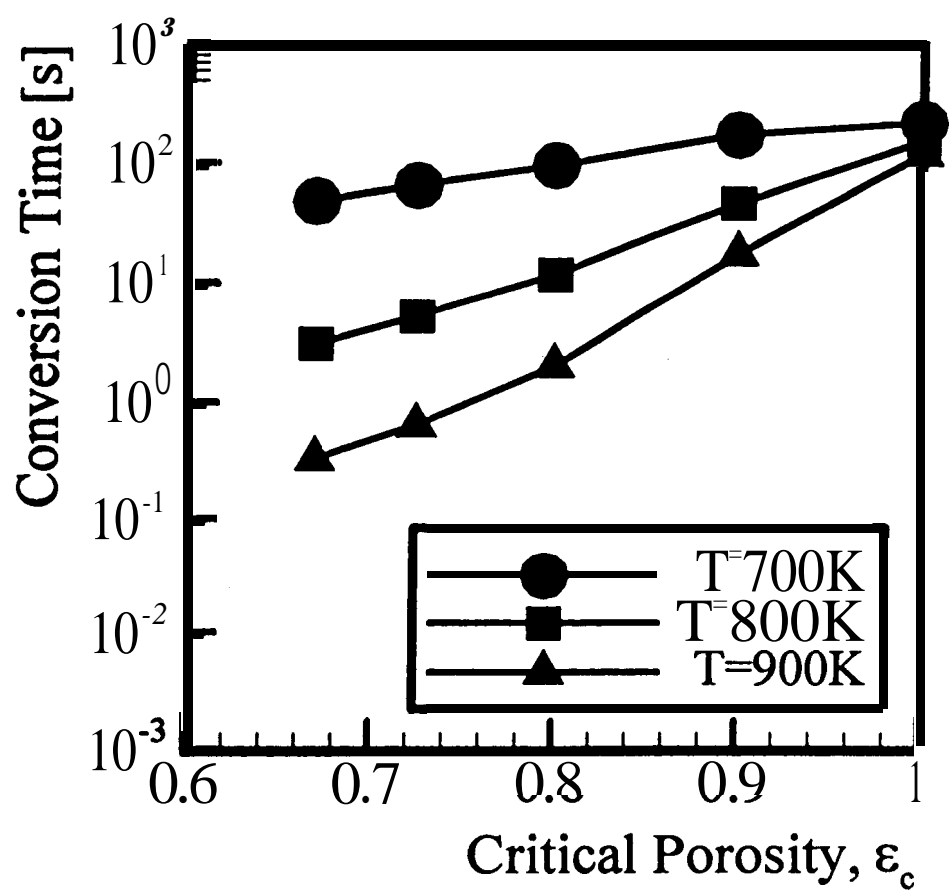
~~7~~



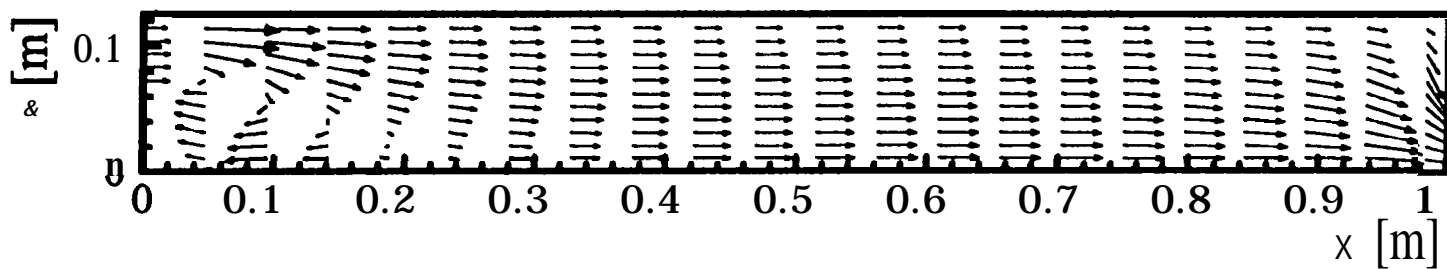




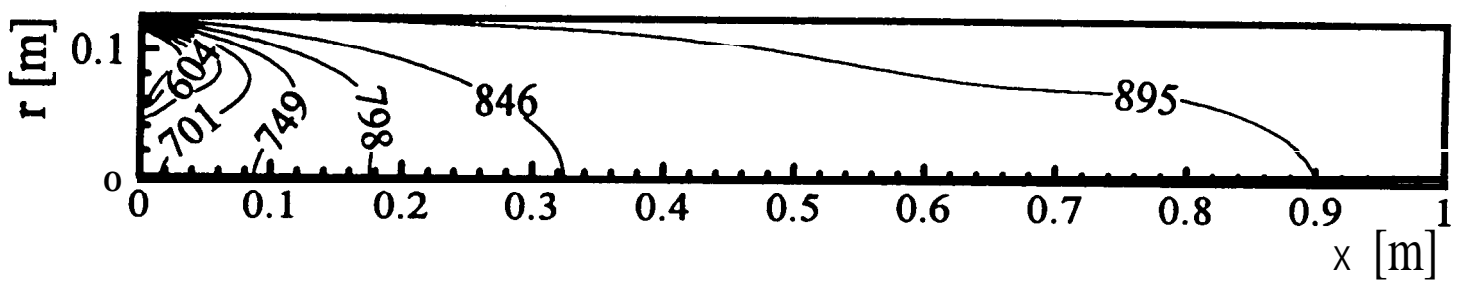
9a



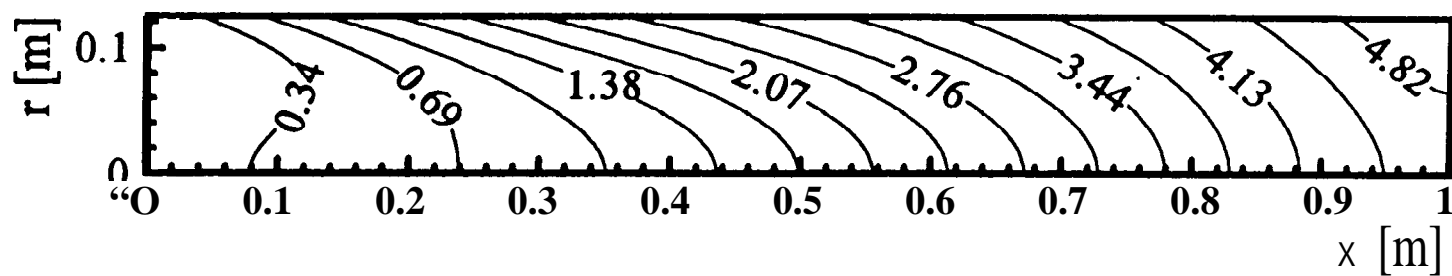
9/6



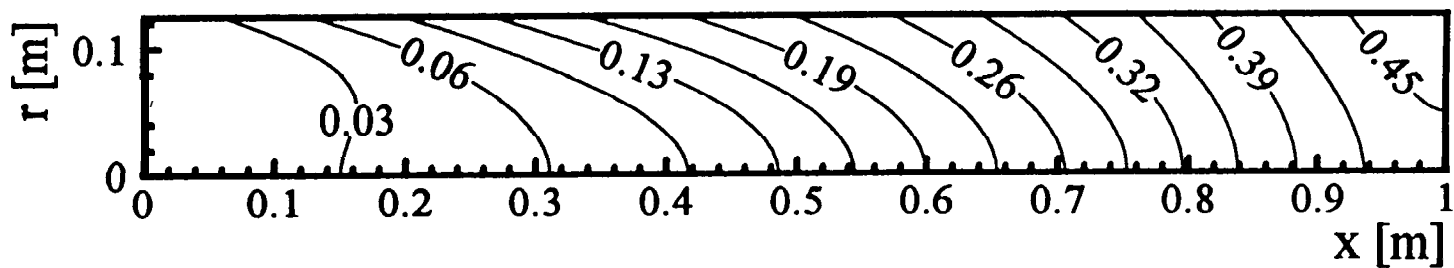
10a



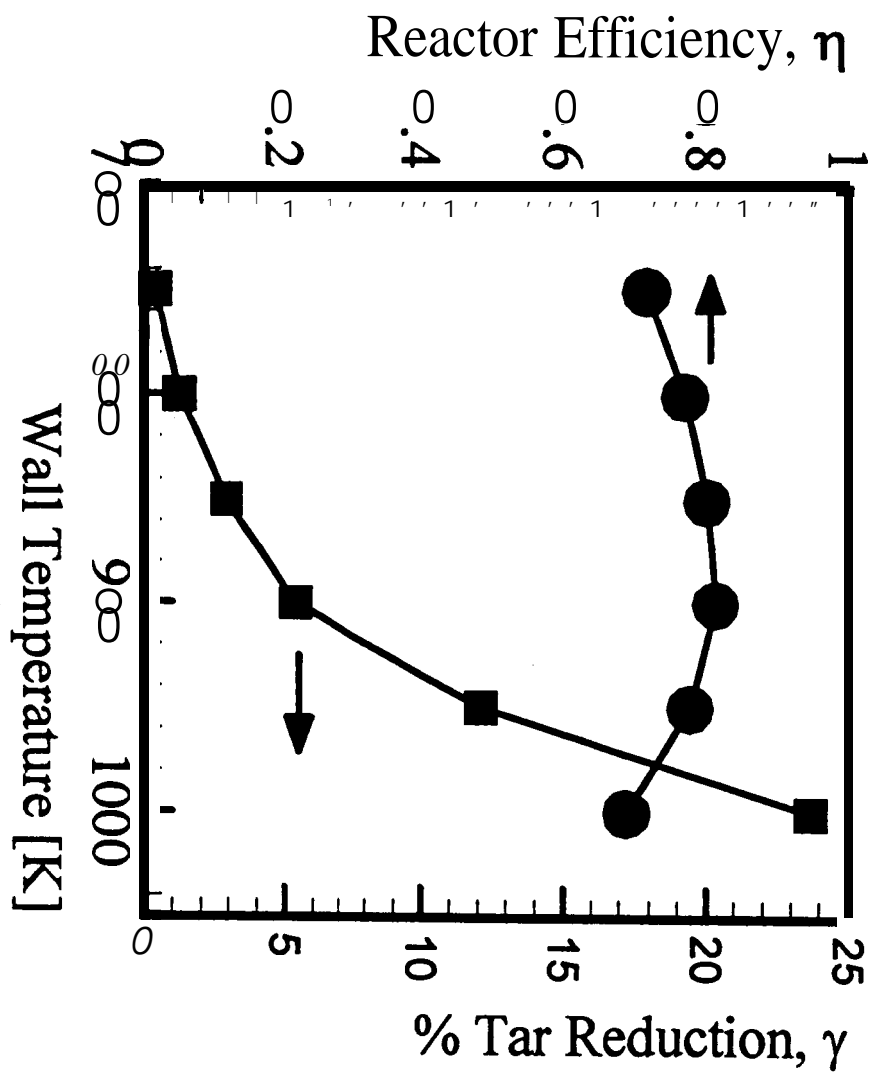
106



10c

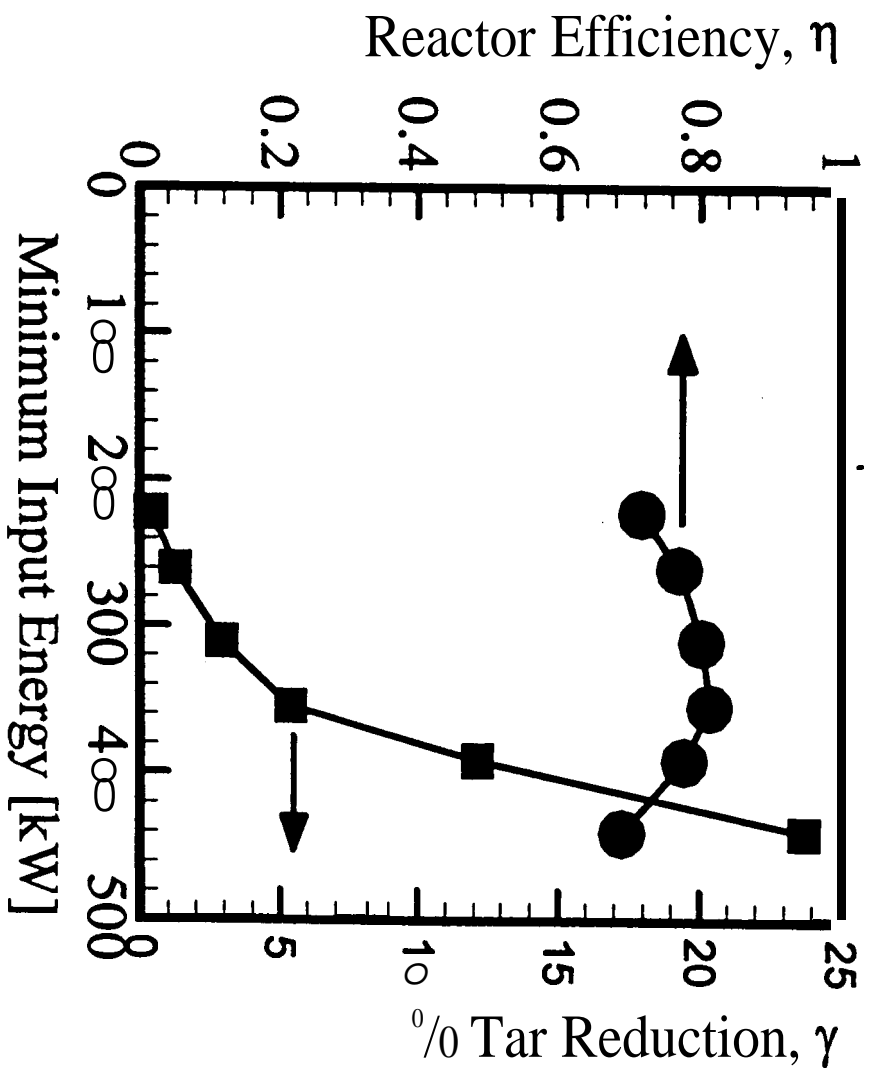


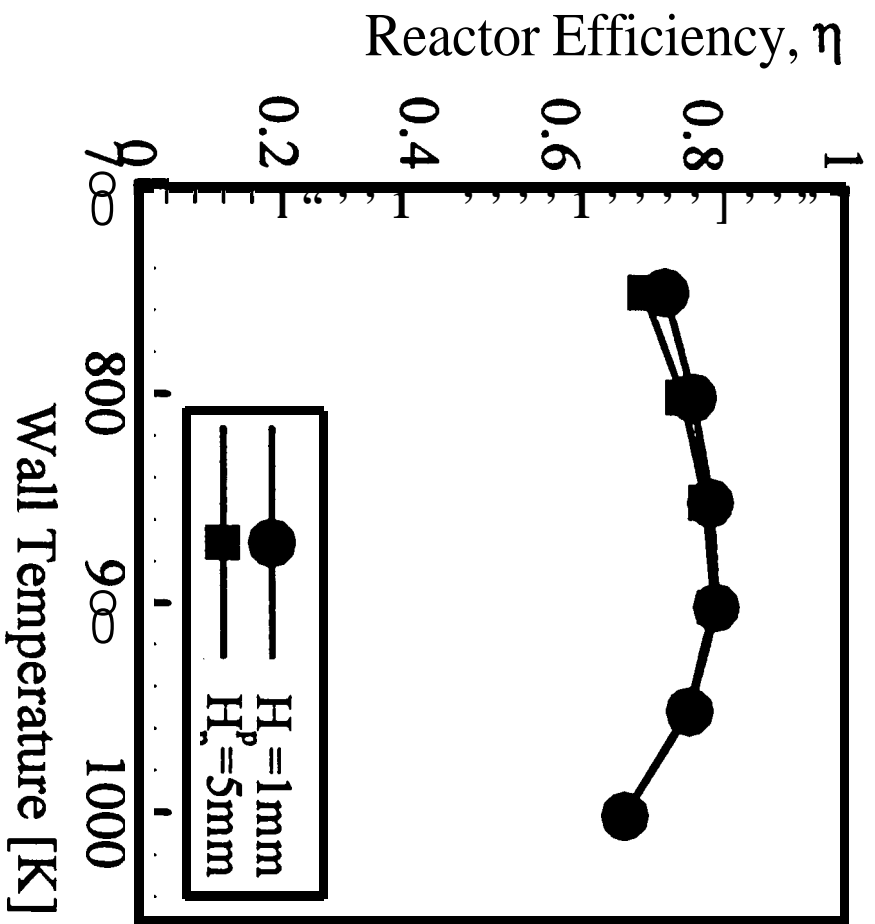
102

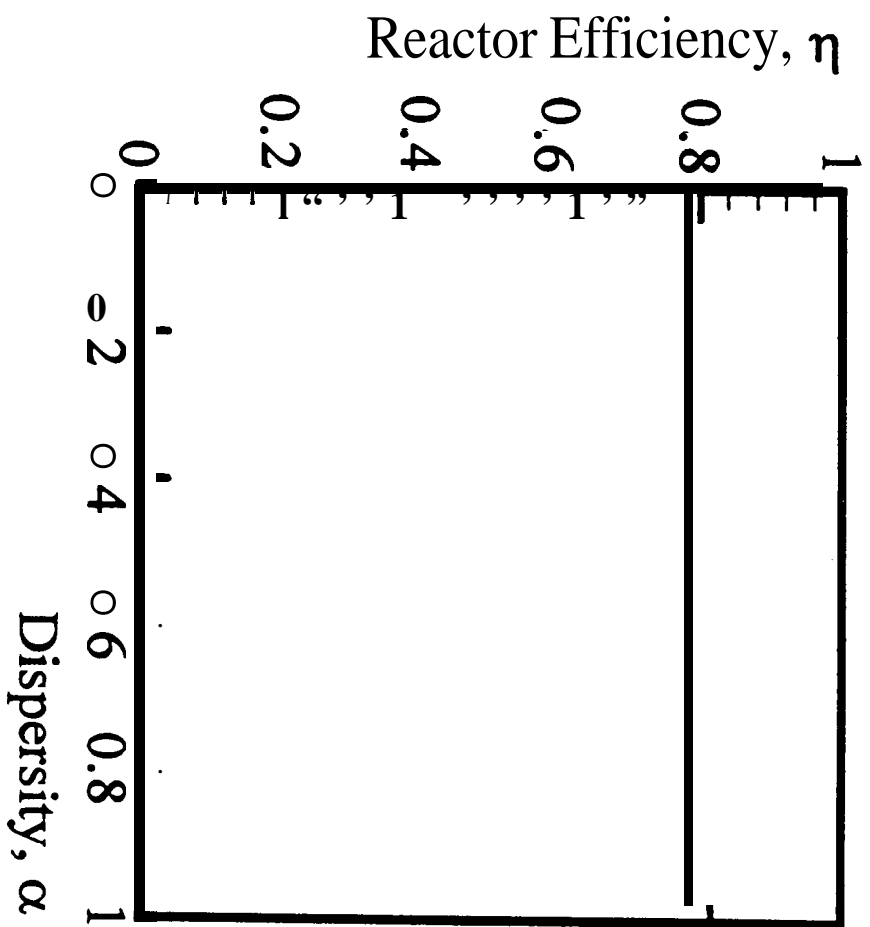


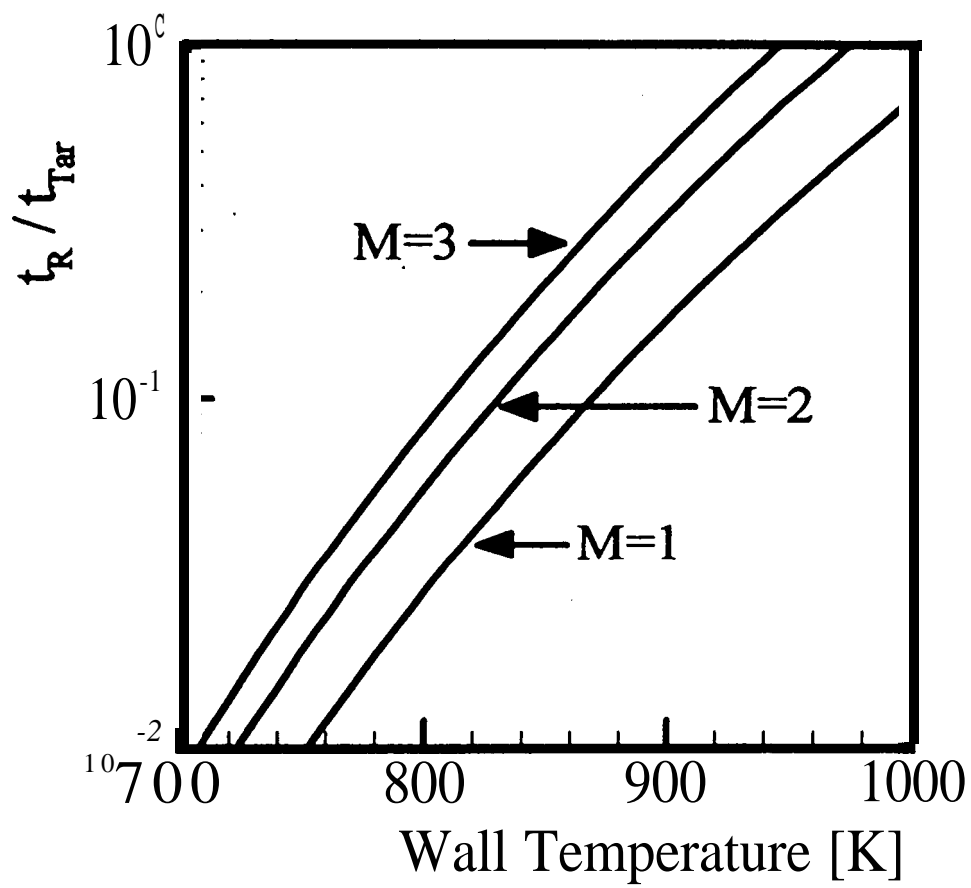
11a

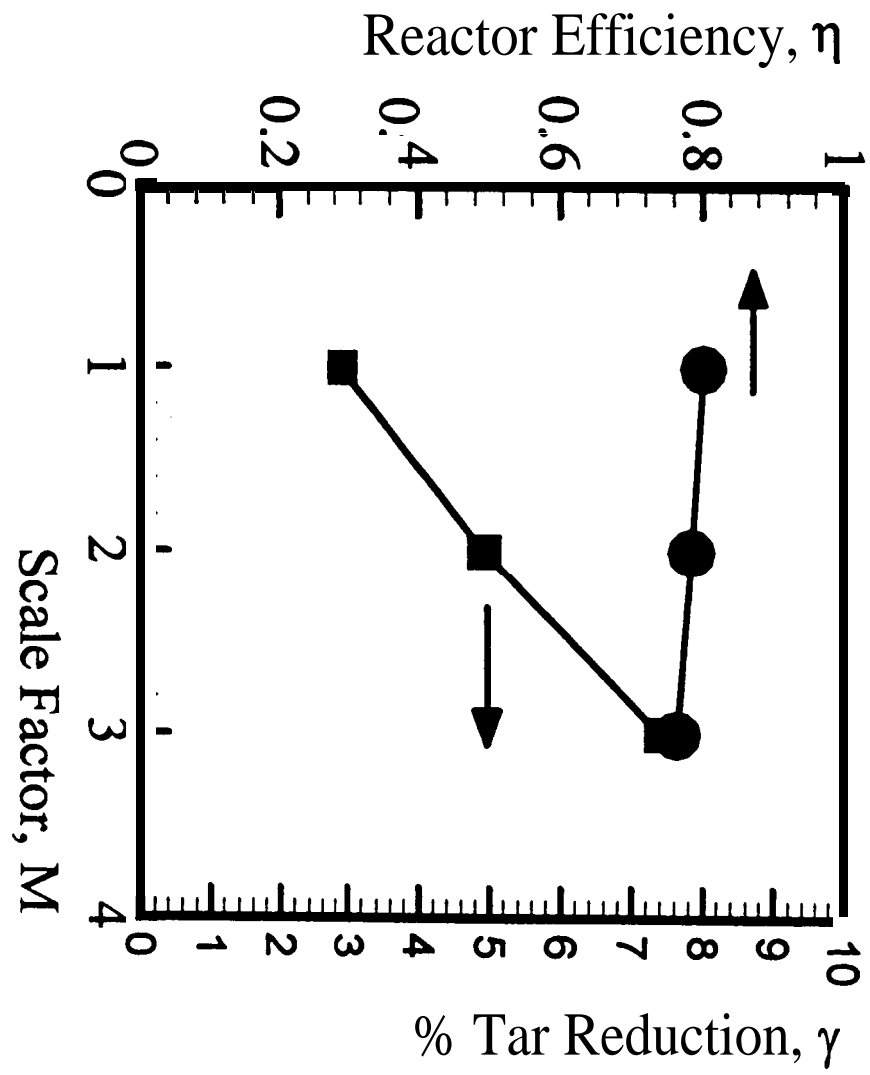












15